Supporting information

Importance of plasma discharge characteristics in plasma catalysis: Dry reforming of methane vs. ammonia synthesis

Robin De Meyer[1, 2, 3], Yury Gorbanev[1], Radu-George Ciocarlan[4], Pegie Cool[4], Sara Bals[2, 3] and Annemie Bogaerts[1]

[1] Research group PLASMANT, Department of Chemistry, University of Antwerp, Universiteitsplein 1, 2610 Antwerp, Belgium
[2] Research group EMAT, Department of Physics, University of Antwerp, Groenenborgerlaan 171, 2020 Antwerp, Belgium
[3] Nanolab Centre of Excellence, University of Antwerp, Groenenborgerlaan 171, 2020 Antwerp, Belgium
[4] Research group LADCA, Department of Chemistry, University of Antwerp, Universiteitsplein 1, 2610 Antwerp, Belgium

Contents

S1. Scanning Electron Microscopy: Determination of radial distribution of WI catalysts

An energy dispersive X-ray spectroscopy (EDX) map is acquired from the cross section of a wet impregnated (WI) bead, covering a large area of the cross section, as illustrated in Figure S1. Then, the center and radius of the bead are determined, after which the EDX-based elemental content can be quantified to yield a radial distribution and overall catalyst loading. To obtain a weight percentage of the catalyst metal (either Ni or Co), the original O signal was neglected and replaced by the stoichiometric amount based on the Al signal, since O is difficult to quantify accurately, and moreover, it was unclear which fraction of O would originate from Ni or Co oxides. In addition to the radial distributions presented in the main text, radial distribution of Ni and Co, respectively, in different beads are shown in Figure S2. The overall loadings (11.1 wt% for Ni and 9.3 wt% for Co) correspond well to the expected 10 wt%.
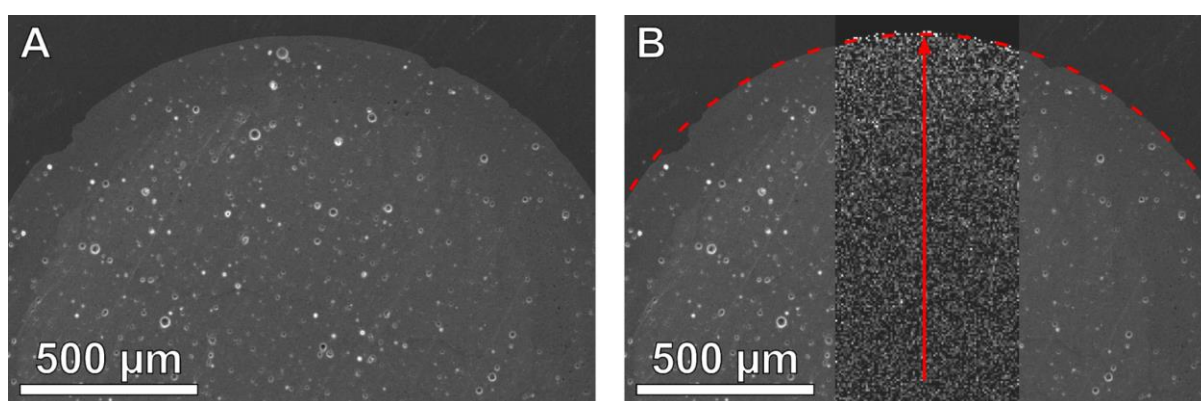

Figure S1: A: Scanning electron microscopy (SEM) image of a cross-section of a WI Co bead, and B: illustration of the quantification of the EDX map (overlaid on the SEM image) to yield a radial distribution of the catalyst
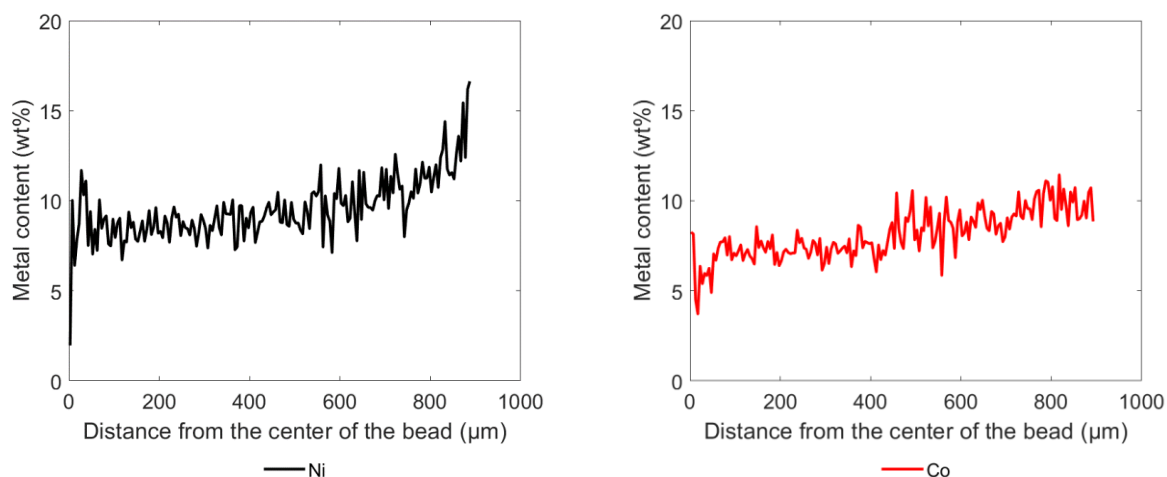

Figure S2: Radial distribution of Ni (left) and Co (right) throughout their respective WI beads. The overall loadings of these samples are 11.1 wt% (Ni) and 9.3 wt% (Co).

S2. Reactor dimensions

The dimensions of the dielectric barrier discharge (DBD) reactor used in this work are presented graphically in Figure S3. The length of the outer electrode is 100 mm (the packing was slightly longer to make sure the discharge only took place around the packing, and not the glass wool that keeps the catalysts in place). The diameter of the central rod is 8 mm, the inner diameter of the alumina tube is 17 mm, and the outer diameter of the tube is 22 mm.
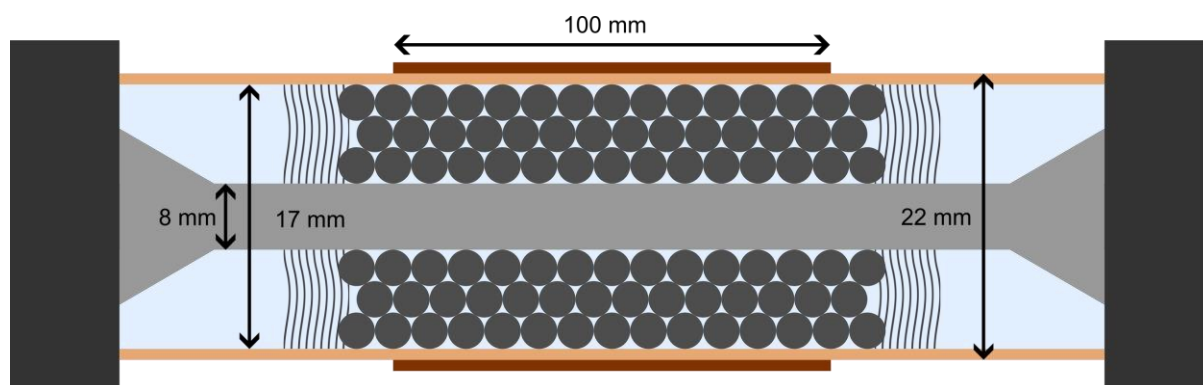

Figure S3: Graphical illustration of the dimensions of the reactor

S3. Evolution of NH$_3$ concentration

An example of the raw data registered by the NH$_3$ sensor in the non-dispersive infrared (NDIR) during an experiment is presented in Figure S4. The NH$_3$ concentration rises steadily and then stabilizes. The average of the signal after stabilization is the original signal which is converted to a true NH$_3$ concentration by using the in-house calibration.

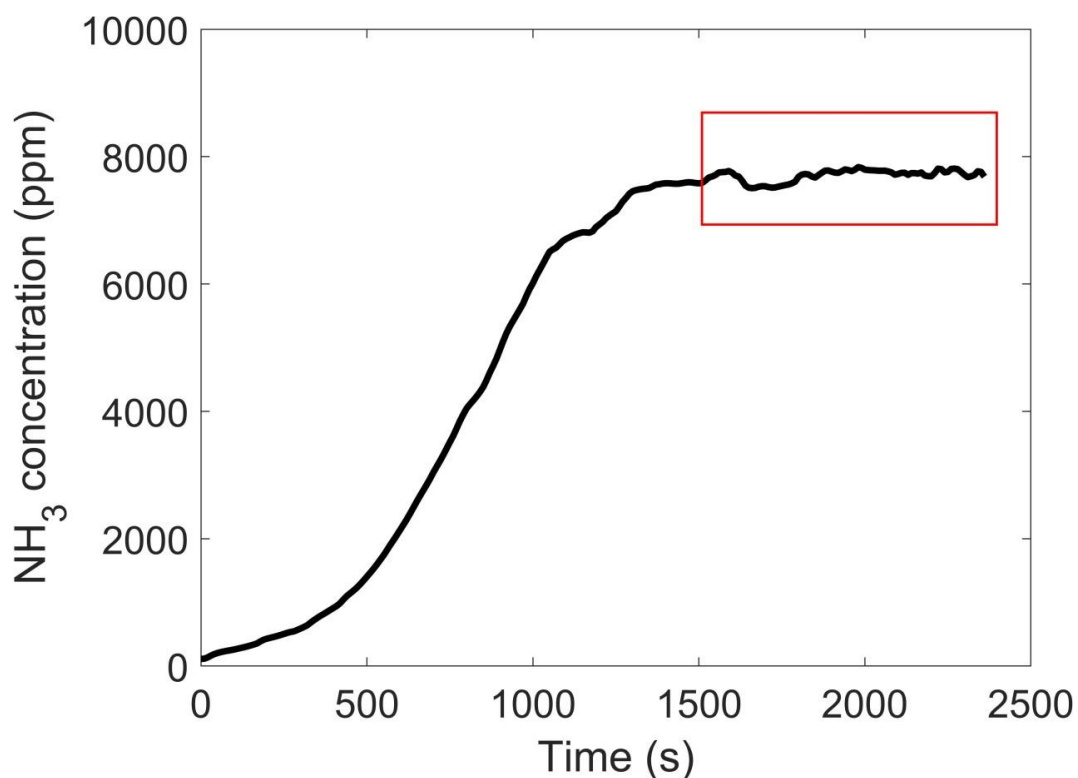*Figure S4: Illustration of the evolution of the NH$_3$ concentration over time. The red box indicates the (quasi-) steady state regime.*

S4.   Comparison of power determination techniques

In this work, the discharge is characterized based on the measurement of the applied voltage and the measured current. These analyses include the plasma power, determined by multiplying the applied voltage with the measured current. A common technique to monitor the plasma power in a DBD is by calculating the area of the Lissajous figure, based on the measured voltage on a monitoring capacitor. The charge on the monitoring capacitor is calculated by multiplying the measured voltage and the capacitance of the capacitor. In this section, we discuss the different techniques and show that in our case, the various techniques yield identical results.

Three techniques to calculate the plasma power are discussed.

(i) Based on applied voltage and measured current ("current1" in Figure S5)

Here, the current measured by the Rogowski coil is multiplied by the applied voltage, to yield a power for every sampling point. These power values are then averaged over one full cycle of the applied voltage (23.5 kHz, i.e. 42.55 µs). Due to some variations in the plasma discharge, the calculated plasma power will vary slightly from one power supply unit (PSU) cycle to the next.

(ii) Based on the area of the Lissajous figure, as calculated from the measured current ("current2" in Figure S5)

The measured current is numerically integrated to yield the charge moving through the system (the best straight fit is subtracted from the integrated signal to ensure an oscillation around zero charge). This charge can then be plotted against the applied voltage to yield a Lissajous figure. The area within the Lissajous figure corresponds to the energy dissipated by the plasma in one cycle. By integrating this area and dividing it by the period of the PSU (23.5 kHz, i.e. 42.55 µs), the power dissipated by the plasma in that cycle can be calculated.

(iii) Based on the area of the Lissajous figure, as measured over the monitoring capacitor ("capacitor" in Figure S5)

The charge moving through the system (as discussed above) can also be measured directly by measuring the voltage over a monitoring capacitor. This again forms a Lissajous figure when plotted against the applied voltage, which is integrated and divided by the period to yield the power.

In one snapshot of the oscilloscope, 11 full cycles are measured, each of which is analyzed separately. The results of the different calculation techniques (based on the same data) are shown in Figure S5. Firstly, it is clear that the power values based on the current data ("current1" and "current2") are very close to each other, showing the accuracy of either calculation method. The power as calculated with "current2" is consistently slightly higher than with "current1", possibly due to a minor error introduced by the different numerical approach of the calculations. The power values based on the measurements over the capacitor are consistently (but only slightly) higher than the ones calculated using the signal generated by the current monitor. However, it is important to note that the cycle-by-cycle variation of the power is much greater than the systematic deviation between these values. This systematic difference could be caused by a tolerance of the capacitance value, meaning a slightly different capacitance than specified by the manufacturer. Indeed, the used capacitor has a capacitance of 10 nF with a tolerance of 1%, which could explain the systematic deviation of approximately 0.7 %.
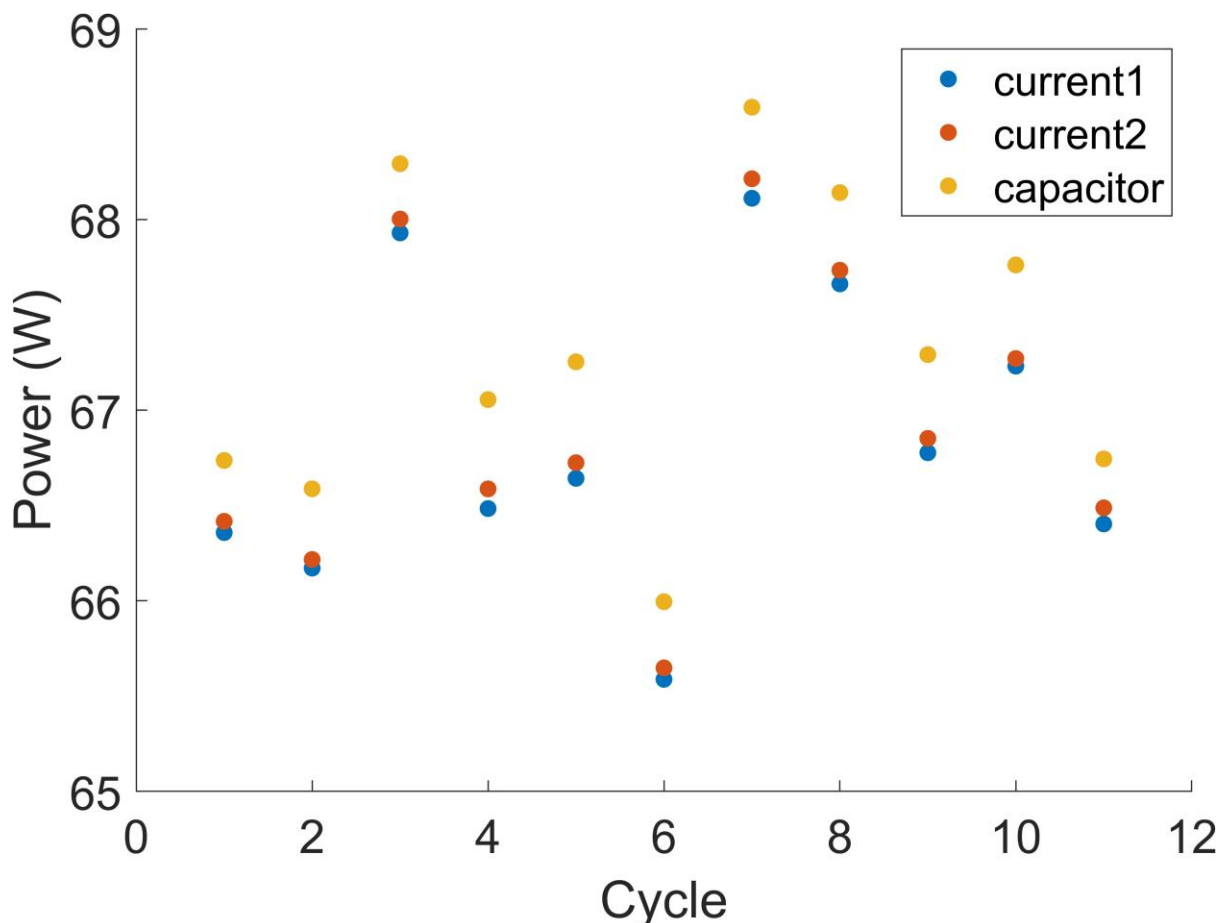
Figure S5: Dissipated power per cycle in one snapshot, calculated using different methods. The cycle-to-cycle variation (due to inherent variation of the plasma discharge) is much larger than the deviation between different calculation techniques. The capacitor technique always yields a slightly higher power than the other techniques, which could be due to a small inaccuracy of the capacitance.

S5. Comparison of Lissajous analysis techniques

As mentioned in the main text, the Lissajous figures are analyzed individually (i.e., corresponding to a single PSU cycle), after which the extracted parameters are averaged ("cycle-by-cycle" analysis). The extracted parameters are then further processed to determine all physical properties, as described in the main text. It should be noted that the interpretation of the Lissajous figures is based on equivalent circuits, which implies a macroscopic approach. However, the extracted values based on the cycle-by-cycle analyses were found to be practically identical to analyzing a single averaged Lissajous figure (average based on all full PSU cycles in one oscilloscope snapshot).

Three illustrative examples are presented here (Figure S6 and Table S1), where the values obtained using the cycle-by-cycle analysis are compared with the values from the averaged Lissajous analysis. These data are all acquired during experiments with a 1:1 gas ratio (CO_2:CH_4 for DRM, and N_2:H_2 for NH_3 synthesis). Visually, the averaged Lissajous figures (Figure S6 A, C, E) are highly similar to the single "raw" Lissajous figures (Figure S6 B, D, F), with only minor smoothing observed for the empty NH_3 case. More importantly, the quantitative extracted characteristics are practically identical, as evidenced by the relative errors in Table S1. Since the errors are all well below 1%, we conclude it is a fair approach to analyze the individual Lissajous figures and average the extracted parameters per experiment. Note that this isn't necessarily true in all cases, since stochastic microscopic events can alter the observed Lissajous figures. However, it seems that in our case, the system is large enough to naturally "average" these microscopic processes, which allows us to interpret and analyze the

individual Lissajous figures as well. If this would not be the case, the Lissajous figures should be averaged prior to analysis.
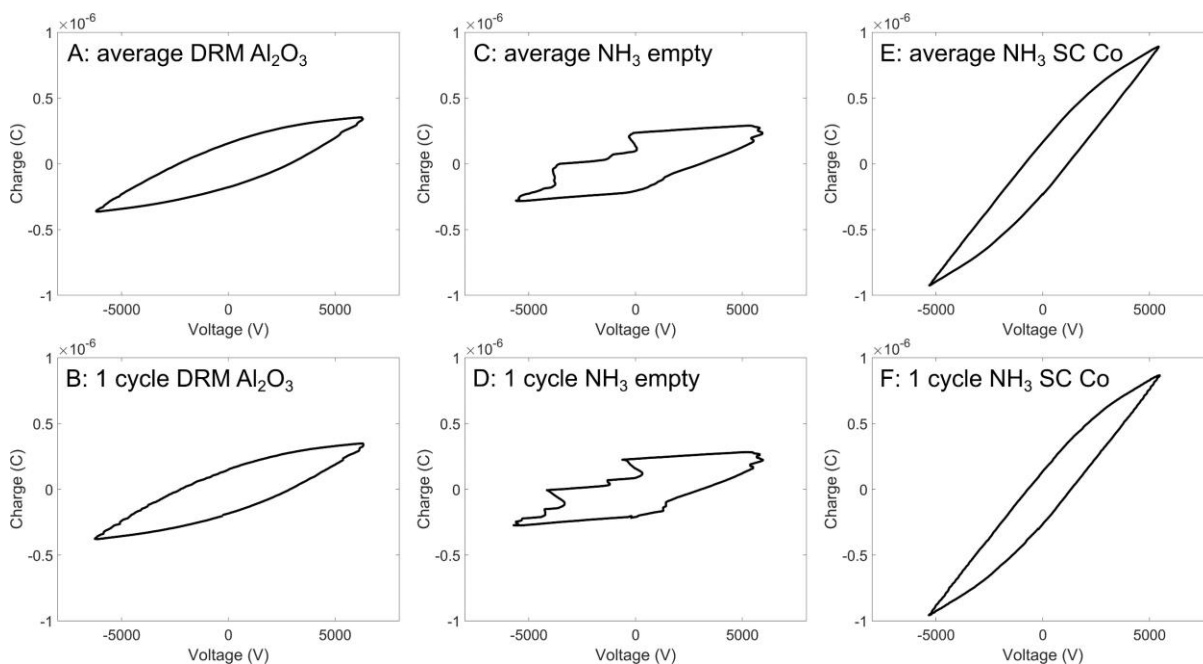

Figure S6: Comparison between averaged Lissajous figures (A, C, E) and single "raw" Lissajous figures (B, D, F). Note that all experiments were performed with a 1:1 feed gas ratio. The extracted parameters from these Lissajous figures are presented in Table S1.

Table S1: Extracted values from Lissajous figures, either based on the average Lissajous figure, or analyzed cycle-by-cycle. The relative error is dimensionless, and the examples provided below were all from experiments using a 1:1 gas ratio (either $CO_2 + CH_4$ or $N_2 + H_2$). The corresponding Lissajous figures are shown in Figure S6.

DRM blank Al_2O_3	Averaged	Cycle-by-cycle	Rel. error
ζ_{diel} (F)	1.00×10^{-10}	9.95×10^{-11}	0.0070
C_{cell} (F)	2.36×10^{-11}	2.36×10^{-11}	-0.0028
C_{gap} (F)	3.08×10^{-11}	3.10×10^{-11}	-0.0063
V_{pk-pk} (V)	1.25×10^4	1.25×10^4	-0.0012
ΔU (V)	2.61×10^3	2.60×10^3	0.0018

NH₃ empty	Averaged	Cycle-by-cycle	Rel. error
ζ_{diel} (F)	7.18×10^{-11}	7.20×10^{-11}	-0.0026
C_{cell} (F)	1.30×10^{-11}	1.30×10^{-11}	-0.0007
C_{gap} (F)	1.58×10^{-11}	1.58×10^{-11}	-0.0003
V_{pk-pk} (V)	1.16×10^4	1.16×10^4	0.0006
ΔU (V)	3.13×10^3	3.15×10^3	-0.0046

NH₃ SC Co 3.3 wt%	Averaged	Cycle-by-cycle	Rel. error
ζ_{diel} (F)	2.12×10^{-10}	2.12×10^{-10}	0.0003
C_{cell} (F)	1.08×10^{-10}	1.08×10^{-10}	-0.0004
C_{gap} (F)	2.18×10^{-10}	2.19×10^{-10}	-0.0012
V_{pk-pk} (V)	1.08×10^4	1.08×10^4	-0.0001
ΔU (V)	1.01×10^3	1.01×10^3	-0.0009

S6. Determining the plasma current

In order to obtain the true plasma current I_{plasma}, the measured current I has to be corrected by subtracting the capacitive displacement current $I_{displacement}$. Since the DBD is effectively a large capacitor, applying an AC voltage will cause the system to charge and discharge, inducing a consequential current that is also picked up by the current monitor and thus contributing to the measured current I. By assuming the measured applied voltage is indicative of the charge on the capacitor, the change of that voltage over time represents the amount of charge moving around, corresponding to a current. As shown in the main text, this capacitive displacement current is calculated using the following equation:

$$I_{displacement}(t) = C_{cell} \frac{dV(t)}{dt} \tag{1}$$

The C_{diel} value was calculated theoretically, as described in the main text, while the C_{cell} value was extracted from the Lissajous figures. The resulting plasma current I_{plasma} was then analyzed further, as described in the main text in section 2.4, to yield the so-called microdischarge quantity. We take a closer look at this approach and the resulting values in the following supplementary Section S7.

Note that numerically calculating the derivative of the voltage, as is required here, is not straightforward. A high sampling frequency (1.25 GHz) was used during the acquisition of the oscillograms, which is required to capture the microdischarges as accurately as possible. However, the variation of the voltage happens on a much longer timescale than the timestep of these oscillograms. Given the limited bitrate of the oscilloscope (despite some on-device upscaling), this means in practice that there are quite some "plateaus" present in the signal, i.e., tens or even hundreds of subsequent timesteps having identical voltage values. This isn't uncommon, and in most cases doesn't lead to any issues, but it becomes problematic when we attempt to differentiate this signal. Indeed, when calculating the derivative of the raw signal, the points at these plateaus yield a derivative (and thus $I_{displacement}$) of 0, while the points at the edges of the plateaus yield relatively high values for the derivative. This effect is not physical and clearly an artifact of the digital treatment of the analog signal. Therefore, we first apply a moving average filter to the voltage signal to smooth out the plateaus, enabling us to differentiate this smoothed signal which yields a much more sensible result. The window size of this moving average filter was chosen based on the maximum size of the plateaus. All oscillograms were analyzed, storing the maximal plateau widths, which yielded a histogram of all maximal values, shown in Figure S7. Based on this, we decided to apply a window size of 275 timesteps (equivalent to 0.22 µs), to make sure none of the artificial zeros would remain present in the differentiated signal. This smoothing is effectively low pass filtering the signal, which introduces a certain error. However, we assume that given the high capacitance of the system, the momentary dips in voltage due to the microdischarges are still relatively slow (compared to the actual microdischarges) and therefore accurately described despite the smoothed signal. A zoomed-in plot of the raw data, as well as the smoothed signal, is shown in Figure S8. The raw data clearly exhibits the plateaus, which are fully eliminated in the smoothed signal. Further, the smoothed signal only deviates a few V from the raw data, which is negligible on the scale of this signal (peak-to-peak in the order of 10^4 V).

Oscillograms of the measured current and the derived capacitive displacement current for all catalysts are shown in Figure S9 and Figure S11 for DRM and in Figure S10 and Figure S12 for NH_3 synthesis (1:1 ratios), respectively. The calculated plasma current is presented in the main text (Figures 4 and 5).

The correction by subtracting the displacement current sometimes changes the overall shape of the current trace, but the microdischarge behavior (very high frequency components) remain unaffected.
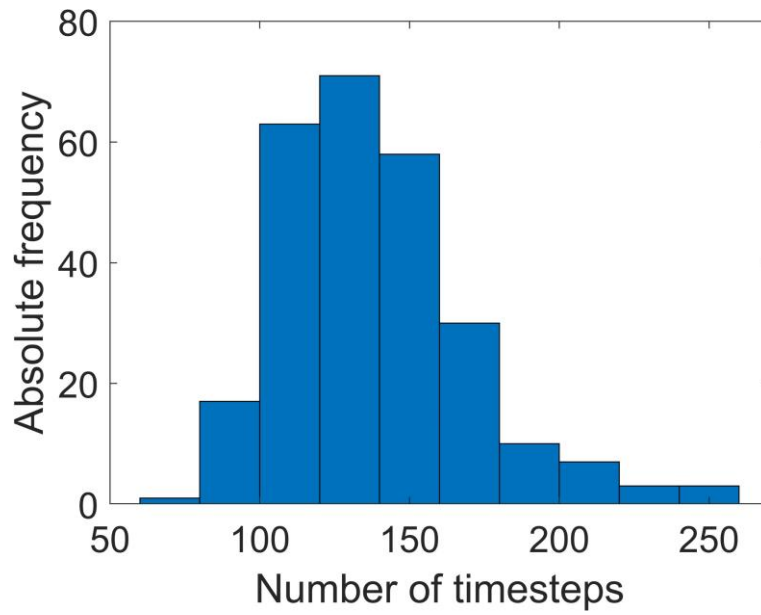
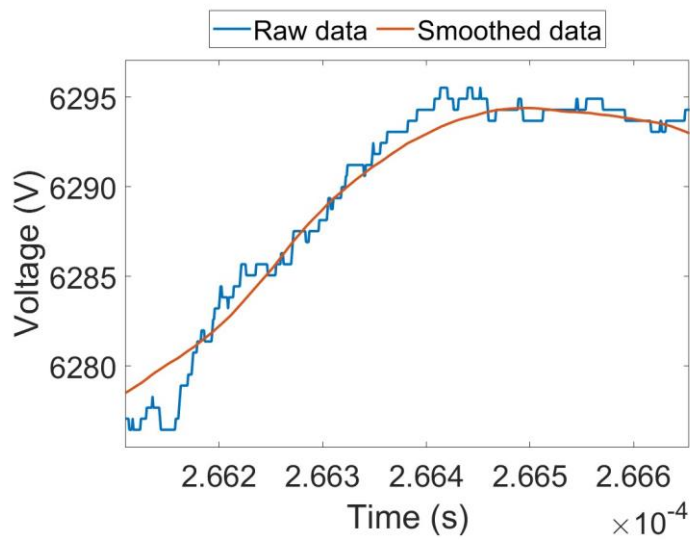*Figure S7: Histogram of all maximal plateau widths*

Figure S8: Raw voltage signal and smoothed signal. The raw data exhibits plateaus in the signal, while these are eliminated in the smoothed signal.
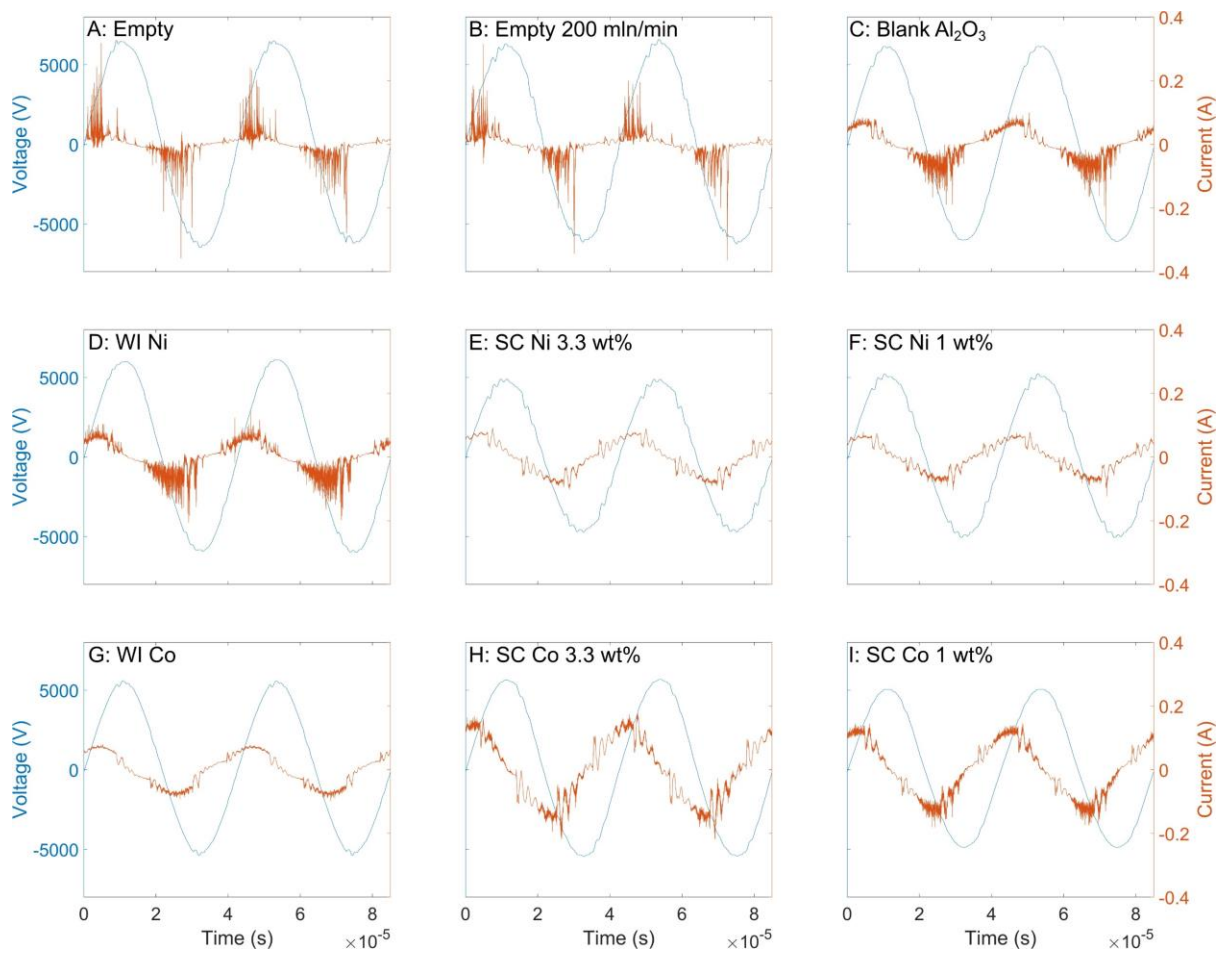
Figure S9: Representative I-V curves of the measured current I for all experimental sets of DRM for a CO_2/CH_4 ratio of 1:1.
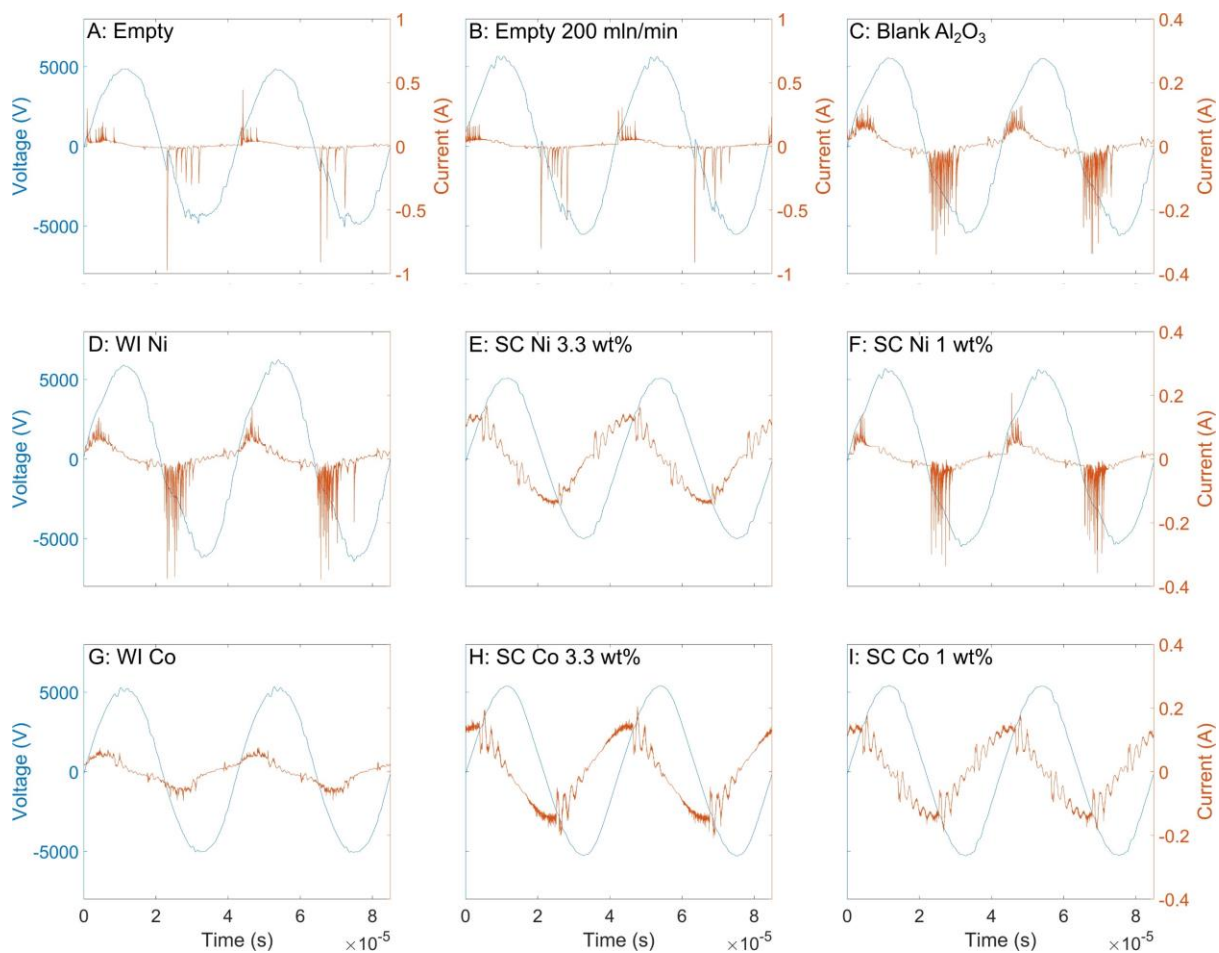
Figure S10: Representative I-V curves of the measured current I for all experimental sets of NH$_3$ synthesis for a N$_2$/H$_2$ ratio of 1:1. Note that the y-axes of the current are wider for the empty reactor at both 100 and 200 mln/min (A,B) compared to the other graphs to prevent clipping the signal while still giving a clear representation of the signal for the other graphs.
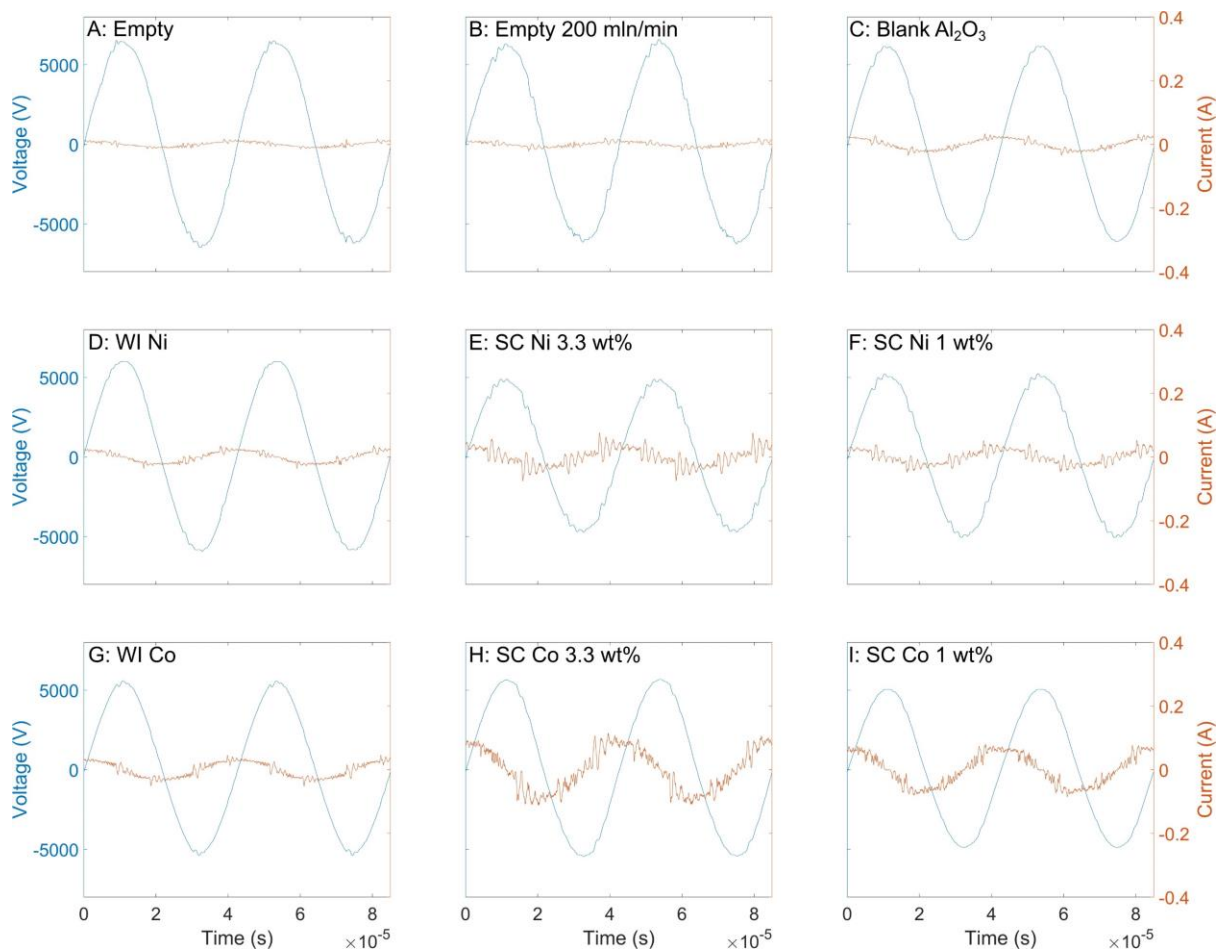
Figure S11: Representative I-V curves of the calculated capacitive displacement current I$_{displacement}$ for all experimental sets of DRM for a CO$_2$/CH$_4$ ratio of 1:1.
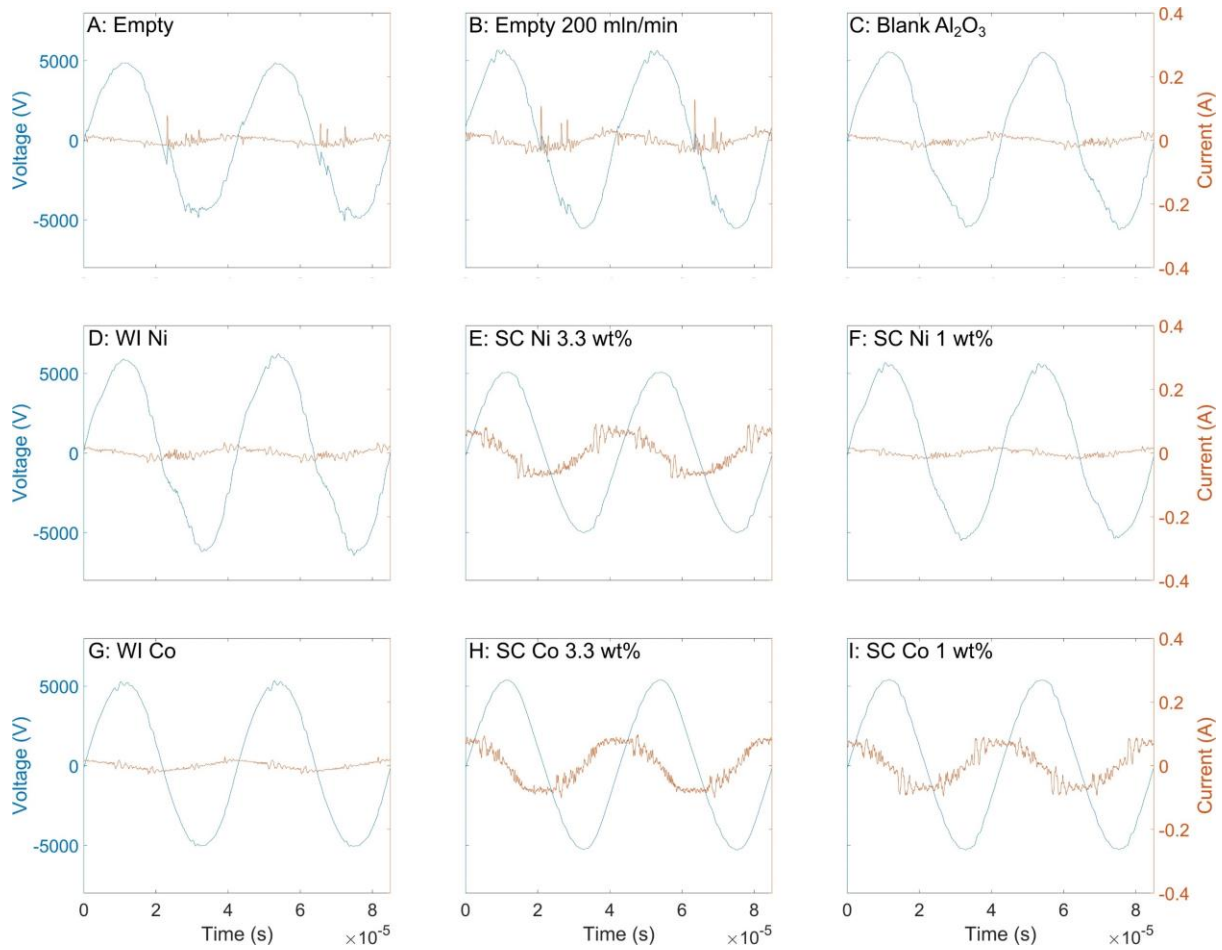
Figure S12: Representative I-V curves of the calculated displacement current $I_{displacement}$ for all experimental sets of NH_3 synthesis for a N_2/H_2 ratio of 1:1.

S7. Microdischarge quantification

The microdischarge quantification starts by determining the capacitive displacement current and subtracting it from the measured current, as described in Section 2.4 of the main text. The resulting signal is the true plasma current I_{plasma}, from which we want to extract information on the microdischarges. As the microdischarges are very intense, but also very short-lived, they can be seen as a high-frequency component superimposed on the lower frequency current variation, provoked by the applied voltage. Roughly, microdischarges last in the order of 10 to 100 ns, which corresponds to a frequency of 10 to 100 MHz. Thus, using this approach, we distill the current signal down to the components corresponding to the 10 to 100 MHz range, and take that as a metric for the so-called microdischarge quantity. Note that both a higher number of microdischarges, as well as a higher intensity of microdischarges, will increase this microdischarge quantity. A part of the information is therefore lost, so the microdischarge quantity should always be used as a supplementary characteristic (in addition to comparing the current traces visually, as well as a detailed study of the Lissajous figures, as described in the main text).

In practice, the calculated plasma current from a full oscillogram is Fourier transformed (FFT), i.e., converted from the time-domain to the frequency-domain. Then, the values within the frequency window of interest (10-100 MHz) are added up to yield the microdischarge quantity. This value does not have a direct physical interpretation, but given an equal data analysis for all experiments, it allows

for a relative comparison between experiments. The standard deviation of this value for different snapshots represents the error bar on the microdischarge quantities.

We compare a few oscillograms with their respective microdischarge quantity, to illustrate how these values can be interpreted. As a first example, we compare the empty reactor with the blank Al_2O_3 experiment for NH_3 synthesis (1:1 ratio) in Figure S13. The microdischarge quantities are 0.737 ± 0.095 and 0.7100 ± 0.0081, respectively. Despite these very similar microdischarge quantities, the plasma current signals are notably different (note the different y-scales). As expected, two different properties of the microdischarges affect this global quantity, i.e., their intensity and their number (per cycle, or their "frequency", though this terminology may be confusing in this context). In the empty reactor, just a few microdischarge occur every half cycle, but each one is very intense. Alternatively, when the reactor is packed with blank Al_2O_3, the number of discharges per half cycle is multiple times higher, but their intensity is much lower. In this case, these two effects compensate each other, leading to these very similar microdischarge quantities. This shows that the interpretation of this value is not straightforward and should always be complemented with additional (qualitative) analyses.
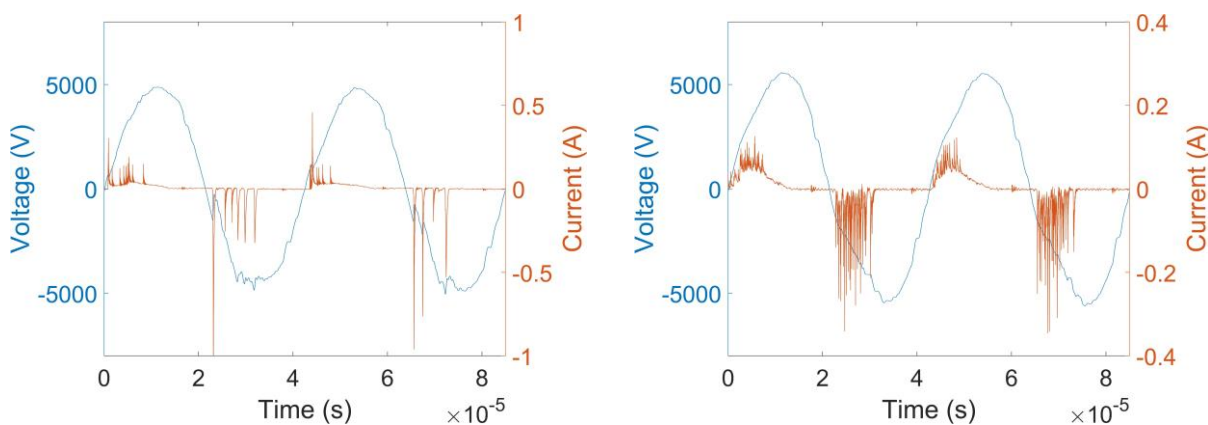

Figure S13: Voltage and plasma current oscillograms for NH_3 synthesis (1:1 ratio) with an empty reactor (left) and a reactor packed with blank Al_2O_3 (right). The corresponding microdischarge quantities are 0.737 ± 0.095 (empty, left) and 0.7100 ± 0.0081 (blank Al_2O_3, right).

However, it is clear that major differences in microdischarge behavior, which may also be easily judged by visual comparisons, are unambiguously demonstrated by the microdischarge quantity as well. For example, when visually comparing the plasma current signals in Figure 4 of the main text (DRM, 1:1 ratio), it is obvious that the WI Ni catalyst exhibits a much higher amount and intensity of microdischarges compared to the SC Ni catalysts. This stark difference is also irrefutably clear in the microdischarge quantity (see also Figure 8 of the main text): 0.782 ± 0.014 for WI Ni and 0.1022 ± 0.0035 for SC Ni 3.3 wt%.

Furthermore, this technique is also capable of picking up smaller, more nuanced differences. For example, when we compare the plasma current signals for NH_3 synthesis (1:1 ratio) for the SC Ni 3.3 wt% catalysts, with the SC Co 3.3 wt% ones (Figure S14), the interpretation of the raw current signal may be less straightforward. The overall shape of the current traces is very similar, but the SC Co one shows some more high-frequency fluctuations, but with a small amplitude, making it tricky to directly interpret. The microdischarge quantity, however, shows a significant difference between these examples, i.e., 0.1479 ± 0.0062 for SC Ni 3.3 wt% and 0.2661 ± 0.0044 for SC Co 3.3 wt%. This indicates that despite the modest amplitude, these features do contribute to the frequencies corresponding to microdischarges, which allows for a more objective and justified interpretation of these results.
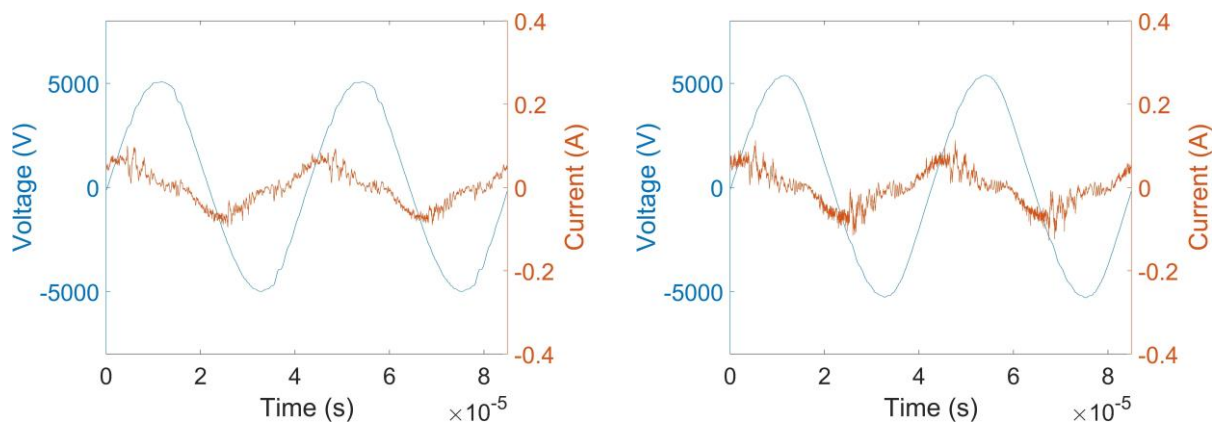
Figure S14: Voltage and plasma current oscillograms for NH$_3$ synthesis (1:1 ratio) with SC Ni 3.3 wt% (left) and SC Co 3.3 wt% (right). The corresponding microdischarge quantities are 0.1479 ± 0.0062 (SC Ni 3.3 wt%, left) and 0.2661 ± 0.0044 (SC Co 3.3 wt%, right).

We believe the strength of this approach is twofold. Firstly, by only looking at the frequencies that are relevant for microdischarges, this analysis immediately eliminates lower frequency current variations. Such lower frequency variations may still occur and can complicate a straightforward visual interpretation, but they are caused by different processes, and thus irrelevant when studying the microdischarge behavior. Secondly, this analysis can be automated easily and is objective, meaning it allows for a facile, straightforward, and direct comparison between experiments, e.g., when comparing different catalysts. As mentioned previously, these results should not be interpreted without any further analysis, but they can serve as a valuable part of the plasma discharge analysis.

S8.   Additional SEM images of SC catalysts

Figure S15 shows additional secondary electron (SE)-SEM images of the cross sectioned spray-coated (SC) catalysts. The Ni or Co layer at the surface corresponds to a thin layer of nanoparticles at the surface of the Al$_2$O$_3$ beads. For the SC Ni catalysts (Figure S15 A-D), the shell is patchy and inhomogeneous, which could be due to a larger detachment of the Ni during manipulation of the beads, or due to a poorer coverage during the synthesis. For the SC Co catalysts (Figure S15 E-H), however, the shell is very homogeneous and uniform, again consisting of nanoparticles. Note that the very bright areas in the SE-SEM images of the Al$_2$O$_3$ support indicate pores, where locally the surface of the material is more or less vertical, allowing many secondary electrons to escape, thus slightly saturating the SE detector.
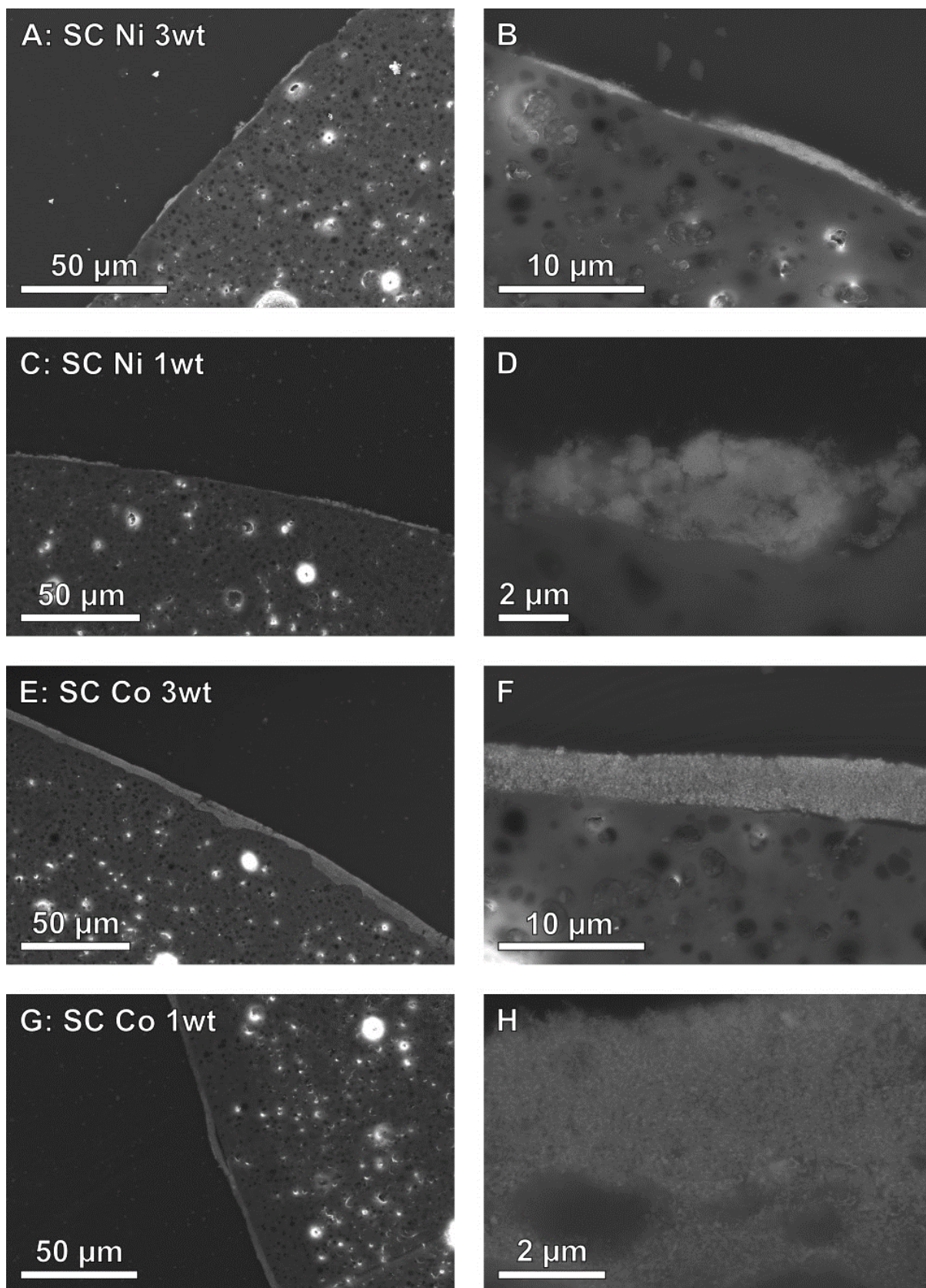
Figure S15: SE-SEM images of the SC Ni 3.3 wt% (A, B), SC Ni 1 wt% (C, D), SC Co 3.3 wt% (E, F), and SC Co 1 wt% (G, H) catalysts.

S9. X-ray powder diffraction

The X-ray powder diffractograms (XRD) of the various Ni- and Co-based catalysts are presented below (Figure S16 for Ni and Figure S17 for Co). Note that while the 10 wt% SC catalysts were not stable enough for reliable plasma catalysis experiments, they are still included in the XRD results. Chemically, they are identical to the catalysts with a lower Ni- or Co- loading, and given their higher loading, the Ni- and Co- based signals are more pronounced.

The WI Ni catalyst shows reflections for Al_2O_3, Ni, and NiO, which indicates an incomplete reduction of the NiO. The SEM-EDX analyses showed that the Ni penetrated to the center of the beads, making those sites harder to reach for the H_2 during reduction, explaining the partial reduction as observed through the XRD data. Similarly, the WI Co catalyst shows reflections for Al_2O_3, Co, CoO, and Co_2O_3. For all SC catalysts, only the metallic phases are represented in the diffractograms, in addition to the Al_2O_3 support.
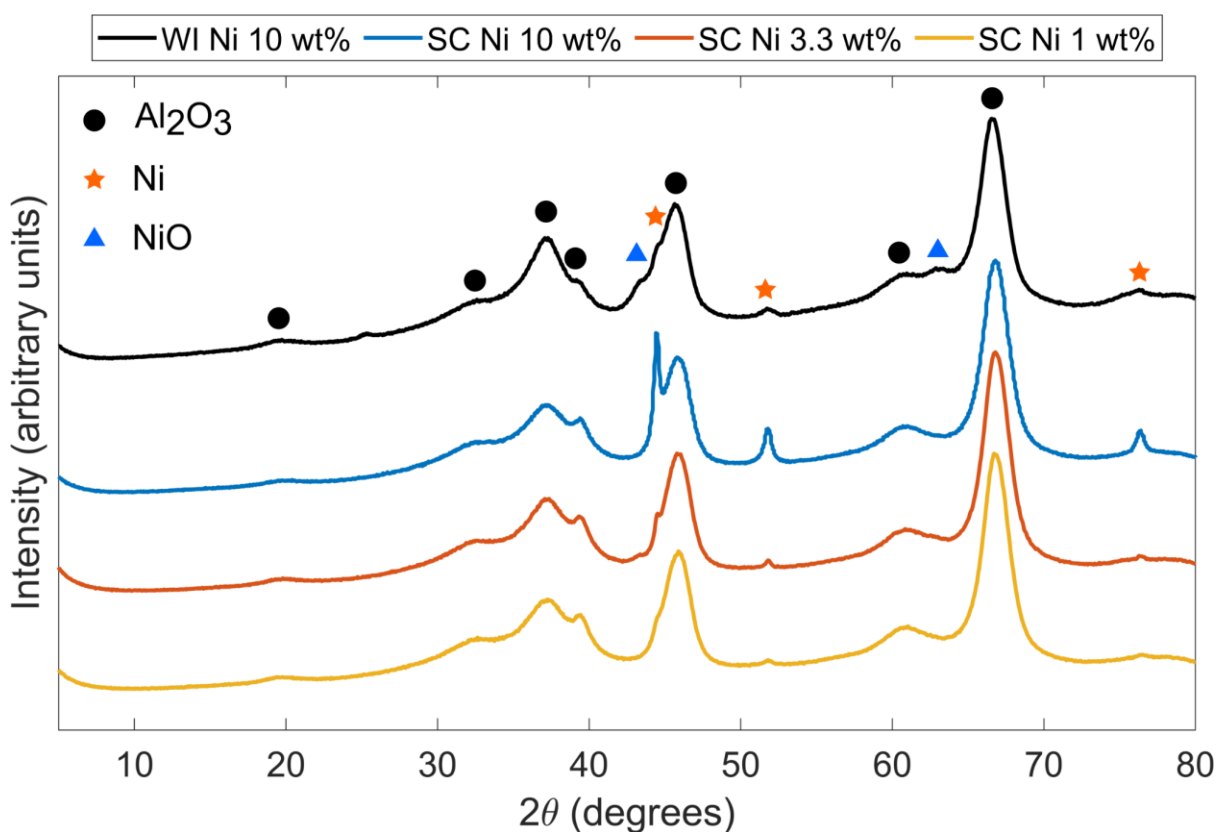
Figure S16: X-ray powder diffractograms for the Ni-based catalysts.
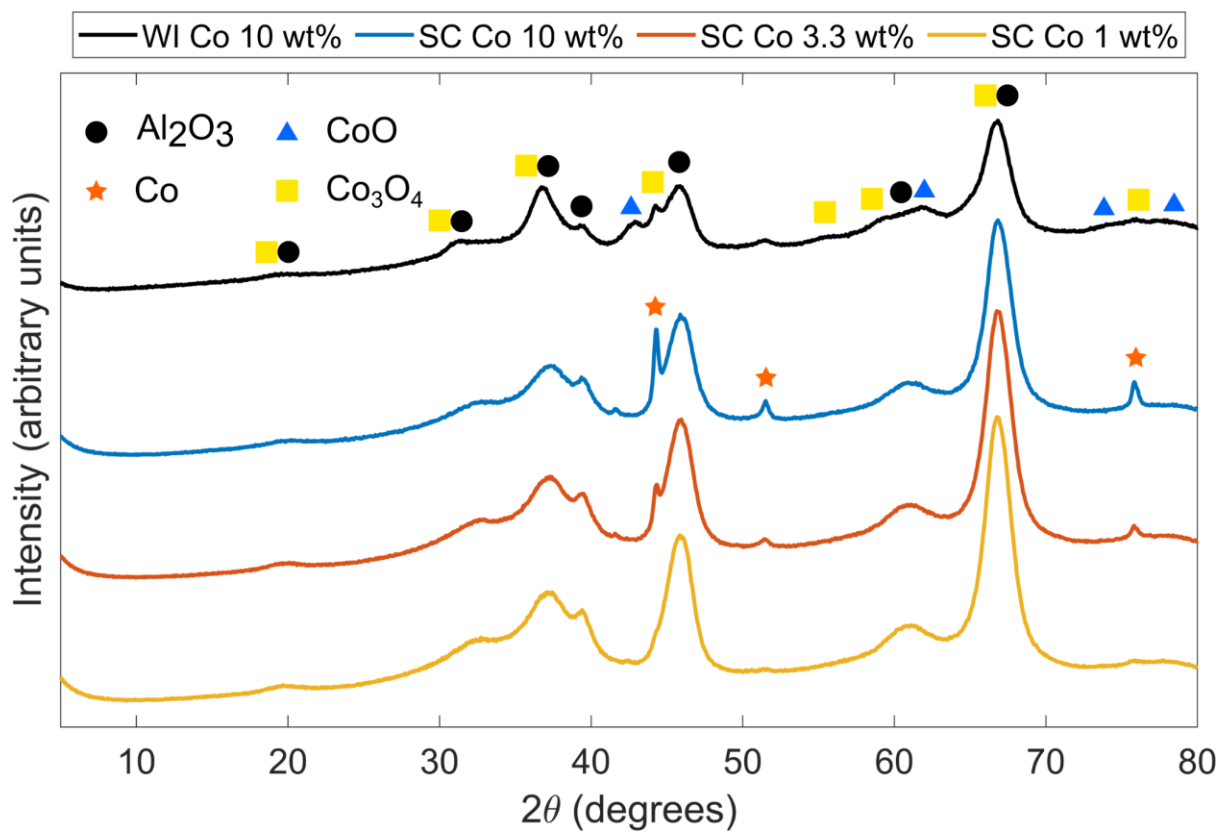
Figure S17: X-ray powder diffractograms for the Co-based catalysts.

S10. Nitrogen sorption

All catalysts were characterized by N_2 sorption at 77 K. All isotherms had the same shape and can all be categorized as IUPAC type IV(a). Some illustrative isotherms are provided in Figure S18. The isotherms were analyzed further to yield a specific surface area for each catalyst, as presented in Table S2. These results are discussed further in the main text.
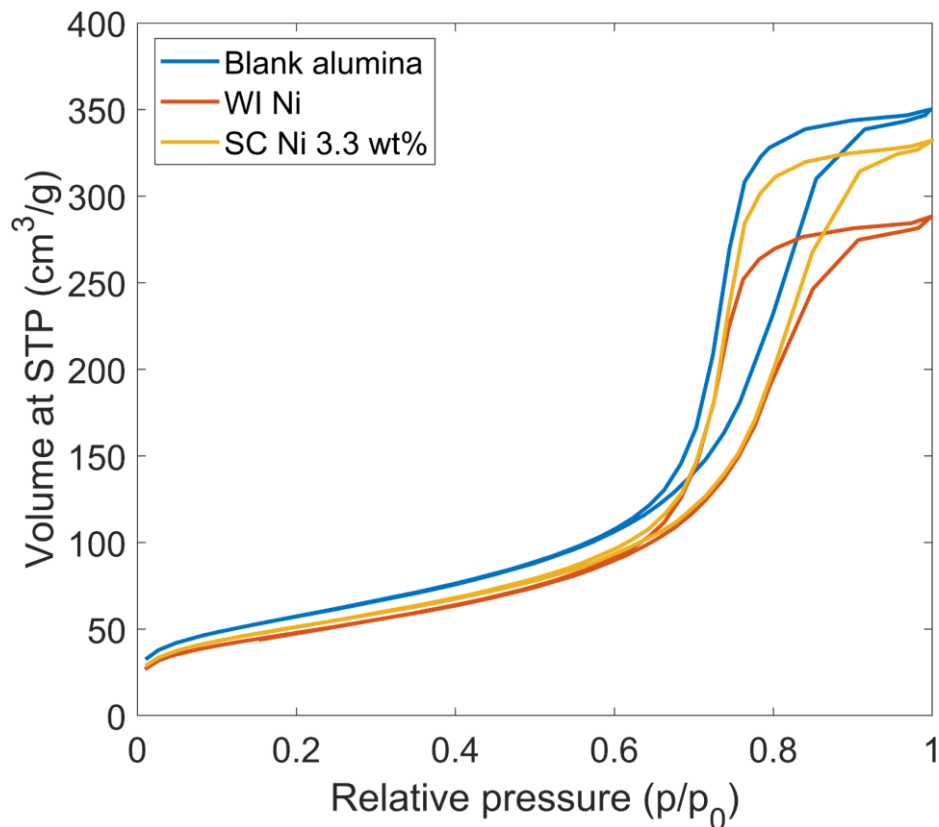

Figure S18: Illustrative N_2 sorption data of the blank Al_2O_3 catalyst, the WI Ni catalyst and the SC Ni 3.3 wt% catalyst. All isotherms have a similar shape, corresponding to the IUPAC type IV(a).

Table S2: Specific surface area of every catalyst, as determined by N_2 sorption.

	BET Specific surface area (m^2/g)
Blank Al_2O_3	244
WI Ni	193
SC Ni 3.3 wt%	202
SC Ni 1 wt%	220
WI Co	183
SC Co 3.3 wt%	211
SC Co 1 wt%	217

S11. Discharge characteristics

Complementary to the electrical characterization presented in the main text, illustrative pictures of the plasma are presented in Figure S19. Here, a clear reactor was built using a quartz tube with similar dimensions to the actual ceramic DBD. These pictures confirm the filamentary discharge for an empty or Al_2O_3 packed reactor, while for a SC Co packed reactor, the plasma becomes more uniform.

Next, various discharge characteristics can be extracted from the current-voltage (I-V) characteristics and Lissajous figures, in addition to those presented in the main text. Here, the peak-to-peak voltage V_{pk-pk}, burning voltage U_b (representing the gap-voltage at the places where discharges occur), cell capacitance C_{cell}, and the conductively transferred charge ΔQ_{dis} are presented for all gas ratios, for both dry reforming of methane (DRM) and NH_3 synthesis (For DRM: see Figure S20, Figure S21, Figure S22, and Figure S23. For NH_3 synthesis: see Figure S24, Figure S25, Figure S26, Figure S27, Figure S28, and Figure S29). Since we aimed for a constant plasma power across the various catalytic experiments, the applied peak-to-peak voltage varies slightly. The applied voltage is the highest for the empty reactor, but this is expected since a higher breakdown voltage is required when no packing is present. The burning voltage U_b, however, does vary significantly between the different catalysts. Especially for the NH_3 synthesis experiments, a high discharging areal fraction β corresponds to a low U_b. This means that while the plasma fills the entire volume of the reactor, the voltage across the gap is relatively low. This will impact e.g. the electron energy, which in turn strongly affects the gas phase chemistry inside the plasma. This is a likely explanation for the good performance in NH_3 synthesis, since the plasma will be less energy-dense, promoting the synthesis of NH_3 rather than its destruction, which is common in the very intense filamentary discharges. Similarly, these catalysts yielding a low U_b also present a high amount of conductively transferred charge ΔQ_{dis}. This makes sense since at lower voltages, a higher current is needed to achieve the same power. This further ties in well with the higher cell capacitance C_{cell} for these "high-β catalysts", since that indicates that the entire system can store more charge at the same applied voltage. The SC catalysts, consisting of a dielectric covered with a conductive layer, can be seen as small capacitors inside the reactor, giving an intuitive explanation for the increased overall capacitance. Interestingly, these trends observed for U_b, ΔQ_{dis}, and C_{cell}, correspond very well with the discharging areal fraction β, indicating that these characteristics are strongly connected and one can likely not be changed without affecting the other. As discussed in the main text, the microdischarges seem to be governed by a different mechanism (illustrated by the WI Co catalyst).

S11.1. Snapshots of plasma discharge

These pictures illustrate the plasma discharge for (A) an empty reactor, (B) a reactor packed with blank Al_2O_3 and (C) packed with SC Co catalysts (3.3 wt%). Note that the presented reactor is not the one that was used for the actual experiments, but rather a prototype using quartz as a dielectric barrier. This reactor was only operated for short periods of time, simply for demonstrative purposes.
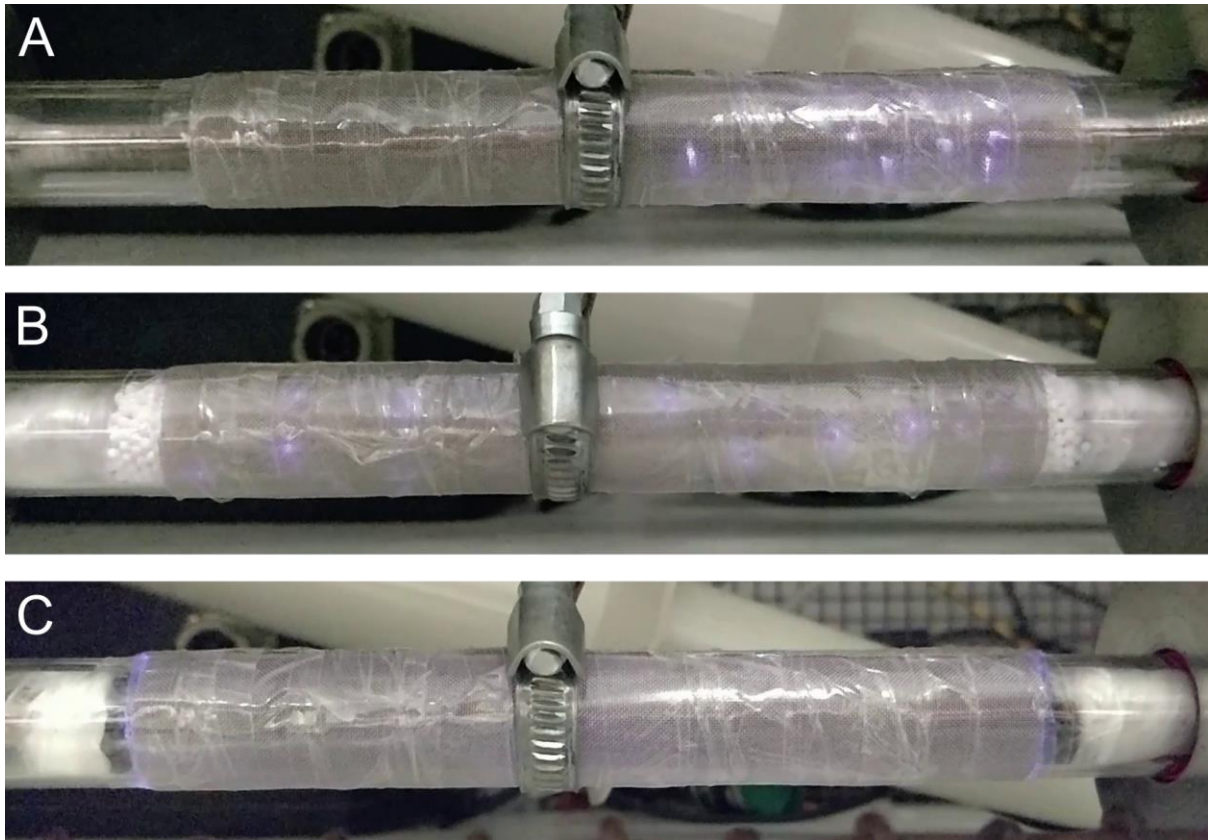
Figure S19: Pictures of a DBD reactor with quartz dielectric (so that the plasma can be visualized), discharging in a N_2/H_2 atmosphere (ratio 1:1). A: empty reactor, B: reactor packed with blank Al_2O_3, C: reactor packed with SC Co 3wt% catalysts. In A and B, the filamentary microdischarges are visible, while in C the plasma is more homogeneous as seen with a uniform purple hue throughout the whole packed bed.
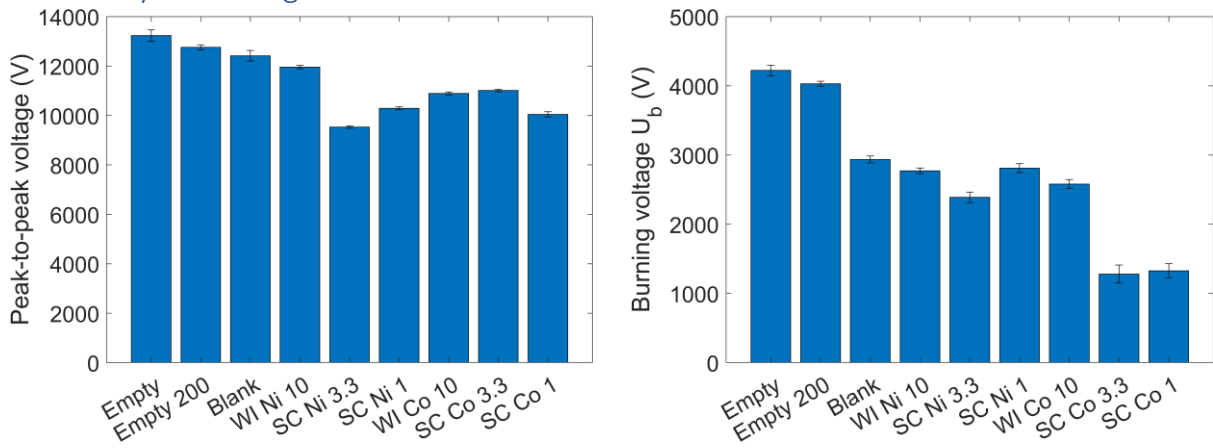
S11.2. Dry reforming of methane

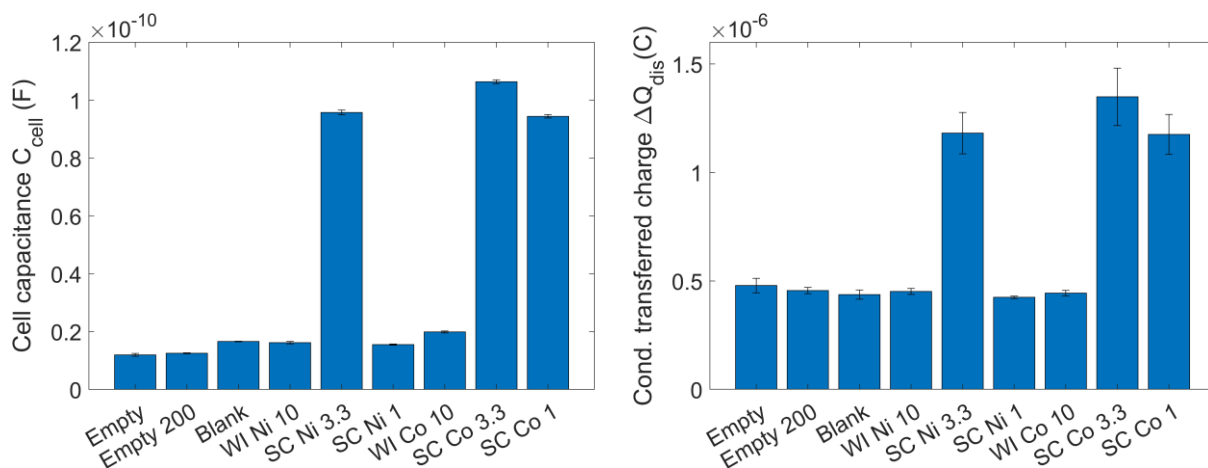*Figure S20: Peak-to-peak voltage (left) and burning voltage U_b (right) for DRM with a CO_2/CH_4 ratio of 1:1*
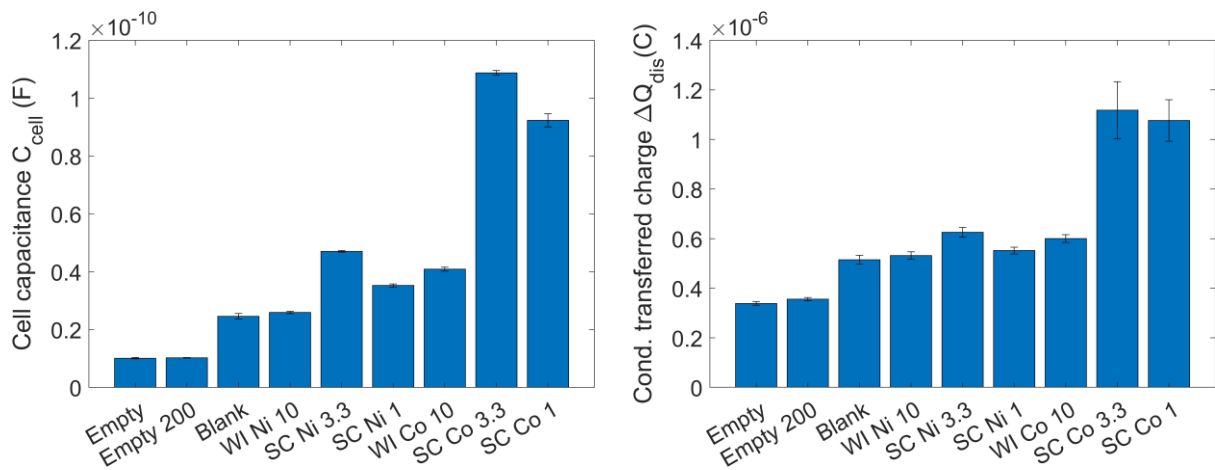
Figure S21: Cell capacitance C_{cell} (left) and conductively transferred charge ΔQ_{dis} (right) for DRM with a CO_2/CH_4 ratio of 1:1
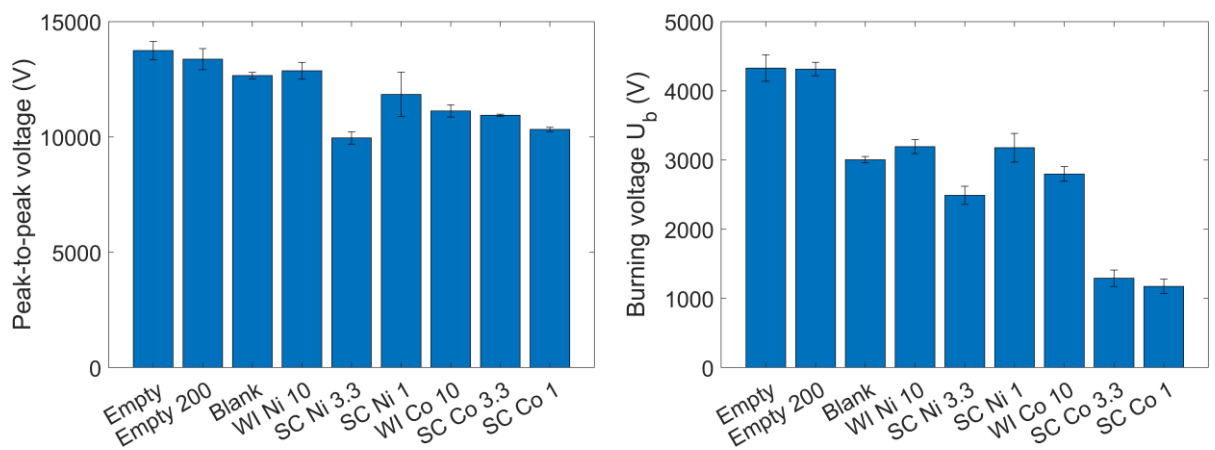
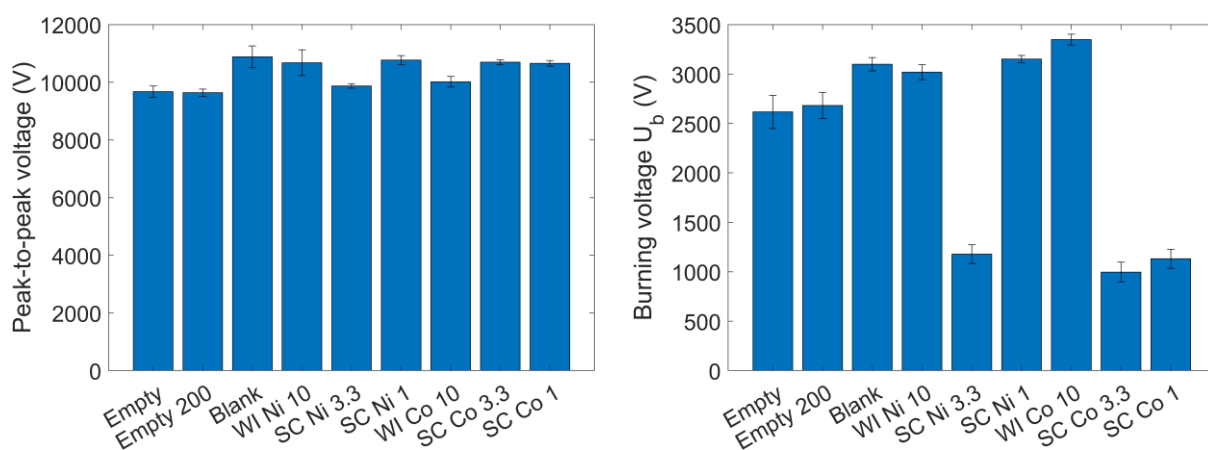Figure S22: Peak-to-peak voltage (left) and burning voltage U_b (right) for DRM with a CO_2/CH_4 ratio of 2:1
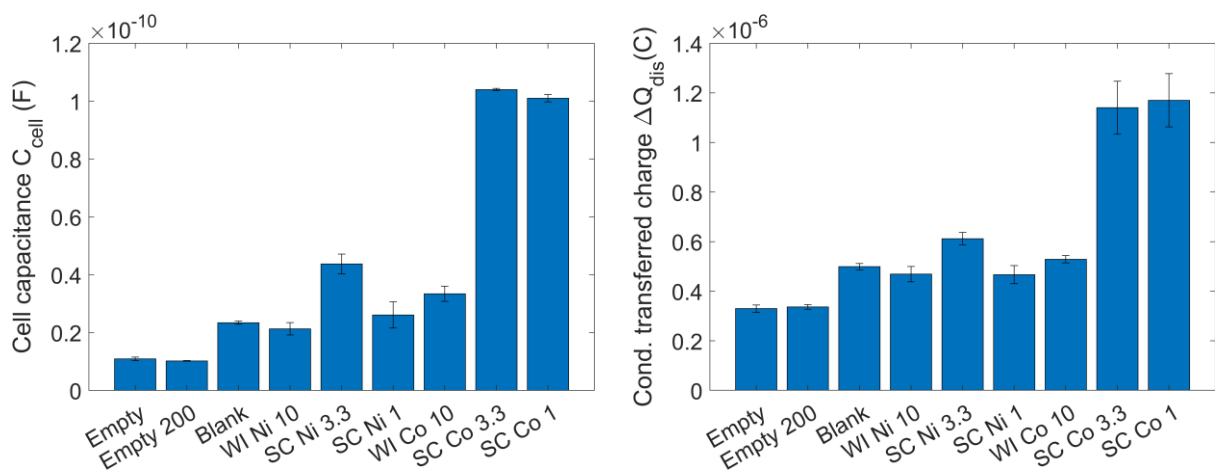
Figure S23: Cell capacitance C_{cell} (left) and conductively transferred charge ΔQ_{dis} (right) for DRM with a CO_2/CH_4 ratio of 2:1

S11.3. NH₃ synthesis
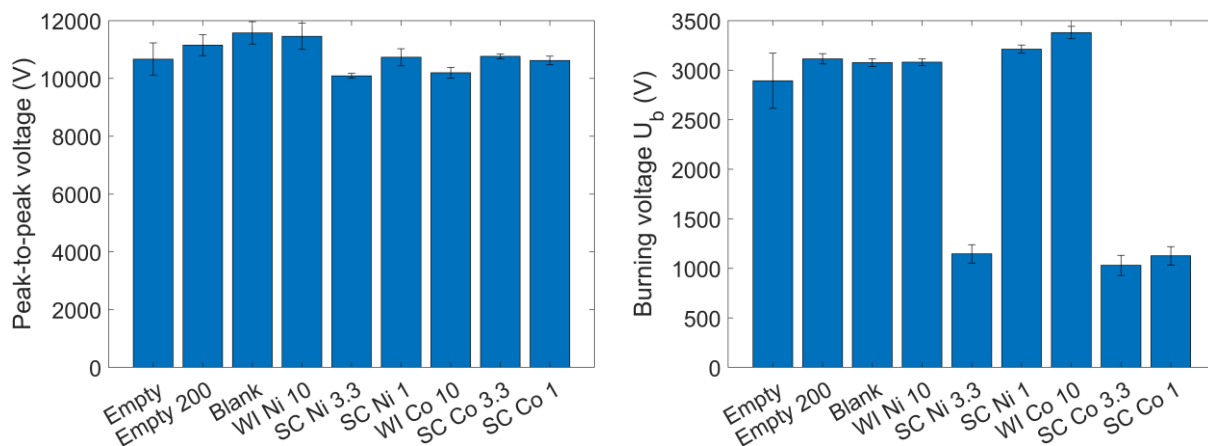
Figure S24: Peak-to-peak voltage (left) and burning voltage Ub (right) for NH₃ synthesis with a N₂/H₂ ratio of 1:1
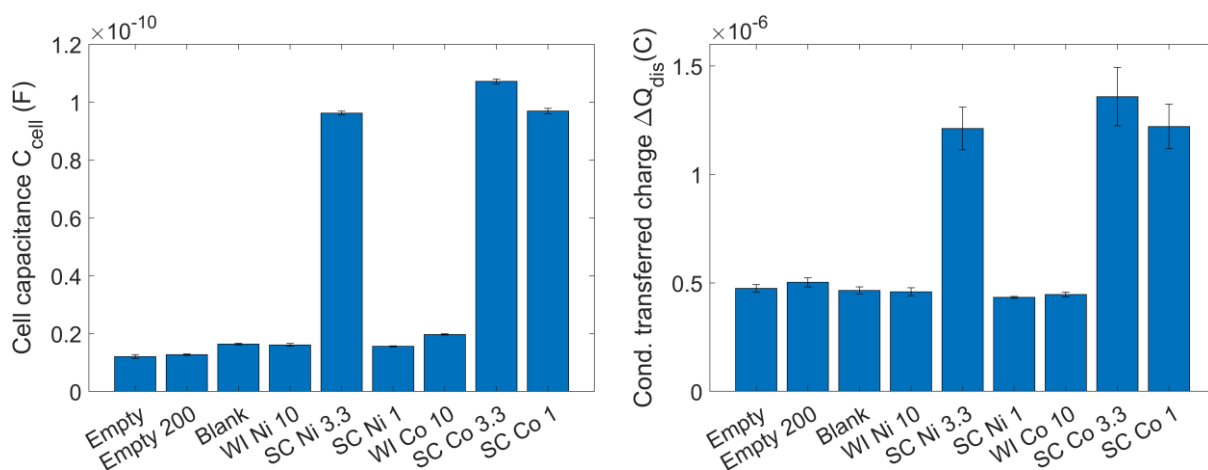
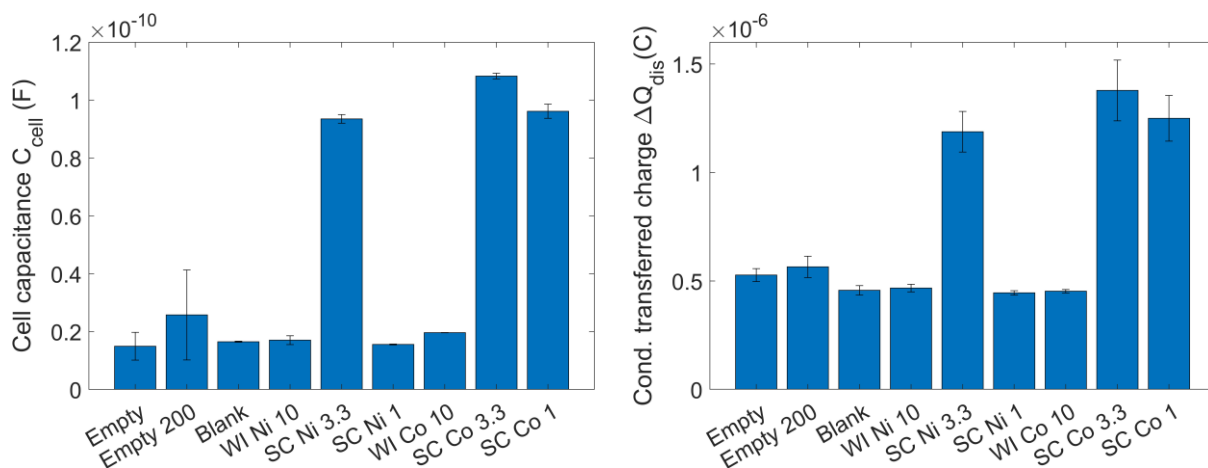
Figure S25: Cell capacitance C_{cell} (left) and conductively transferred charge ΔQ_{dis} (right) for NH₃ synthesis with a N₂/H₂ ratio of 1:1
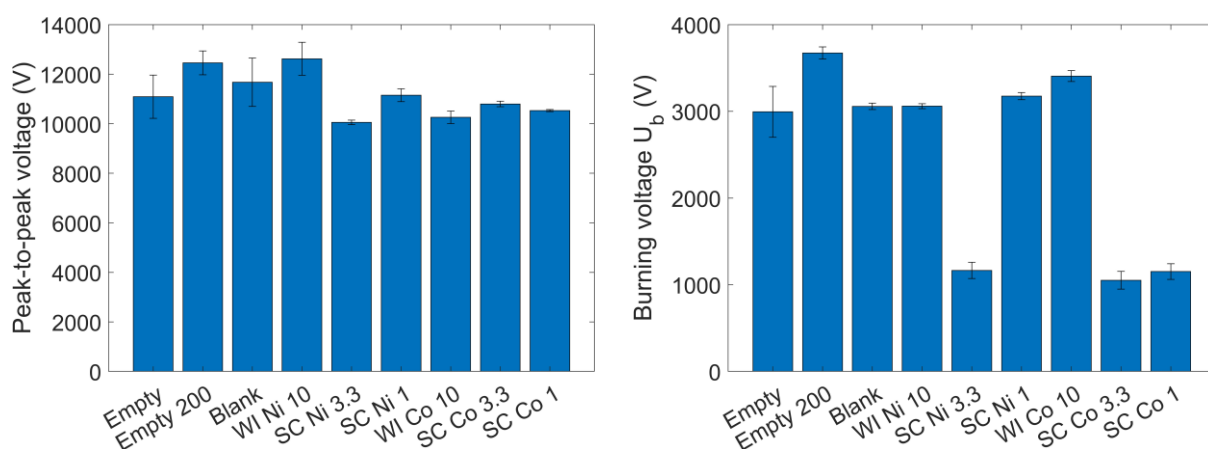
Figure S26: Peak-to-peak voltage (left) and burning voltage U_b (right) for NH₃ synthesis with a N₂/H₂ ratio of 3:1

Figure S27: Cell capacitance C_{cell} (left) and conductively transferred charge ΔQ_{dis} (right) for NH$_3$ synthesis with a N$_2$/H$_2$ ratio of 3:1

Figure S28: Peak-to-peak voltage (left) and burning voltage U_b (right) for NH$_3$ synthesis with a N$_2$/H$_2$ ratio of 1:3

Figure S29: Cell capacitance C_{cell} (left) and conductively transferred charge ΔQ_{dis} (right) for NH$_3$ synthesis with a N$_2$/H$_2$ ratio of 1:3

S12. Additional performance metrics

A number of metrics can be used to describe the performance of the plasma-catalytic experiment. For example, the conversion can be combined with the specific energy input to the system to yield an energy cost (EC, see eq. (12) in the main text). The EC for DRM is shown in Figure S30 and should be interpreted as the amount of energy used for the conversion of CO_2 and CH_4. Figure S36 and Figure S37 show the EC for NH_3 synthesis, which should be interpreted as the amount of energy used for the production of NH_3. As the plasma power for all experiments was very similar, the same trends can be observed as for the total conversion or NH_3 concentration, which are discussed in detail in the main text.

As the chemistry in DRM is much more complicated compared to NH_3 synthesis, a number of additional metrics can be used to analyze the overall performance of this reaction. Firstly, the CO_2 and CH_4 conversions can be considered separately, as presented in Figure S31 and Figure S32 for both CO_2/CH_4 ratios. Again, very similar trends are observed when compared to the total conversion discussed in the main text, with the CH_4 conversion being consistently higher than the CO_2 conversion, attributed to the lower C-H vs C=O binding energy.

Further, the O-based (Figure S33, CO_2/CH_4 ratio of 2:1), H-based (Figure S34, CO_2/CH_4 ratio of 2:1), and C-based (Figure S35, both CO_2/CH_4 ratios) selectivities are presented. The most striking observation here, is that the C_2H_2 selectivities are close to zero for all Ni-based catalysts. This is a clear indication of a chemically-catalytic effect taking place at the metal surface, where Ni has different effects compared to Co, as the discharge characteristics cannot explain this difference. This demonstrates that conventional catalytic effects also exist in plasma catalysis, though, as discussed in the main text, they are certainly not the only reactions taking place, and the gas-phase chemistry determined by the overall plasma discharge cannot be neglected.
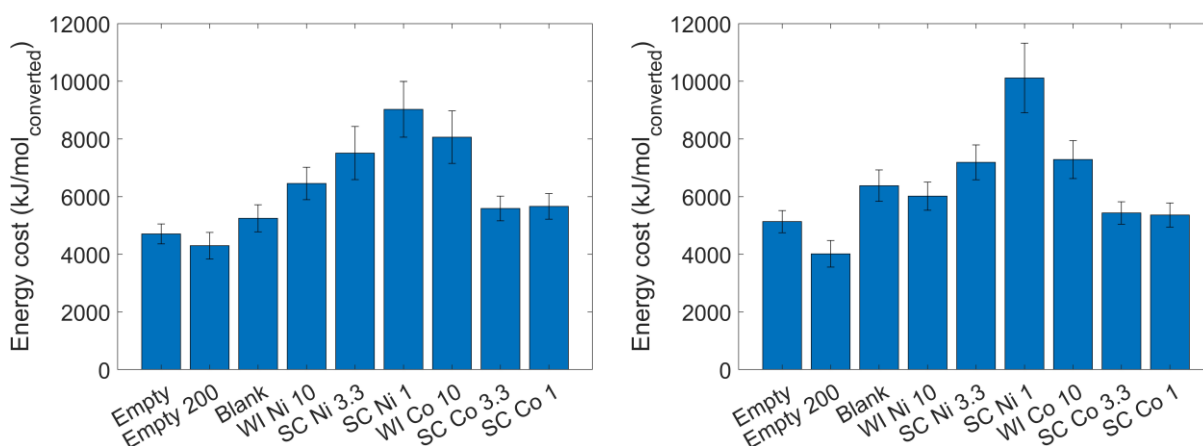
S12.1. Dry reforming of methane

Figure S30: Energy cost (kJ/mol$_{converted}$) for DRM with a CO_2/CH_4 ratio of 1:1 (left) and 2:1 (right)
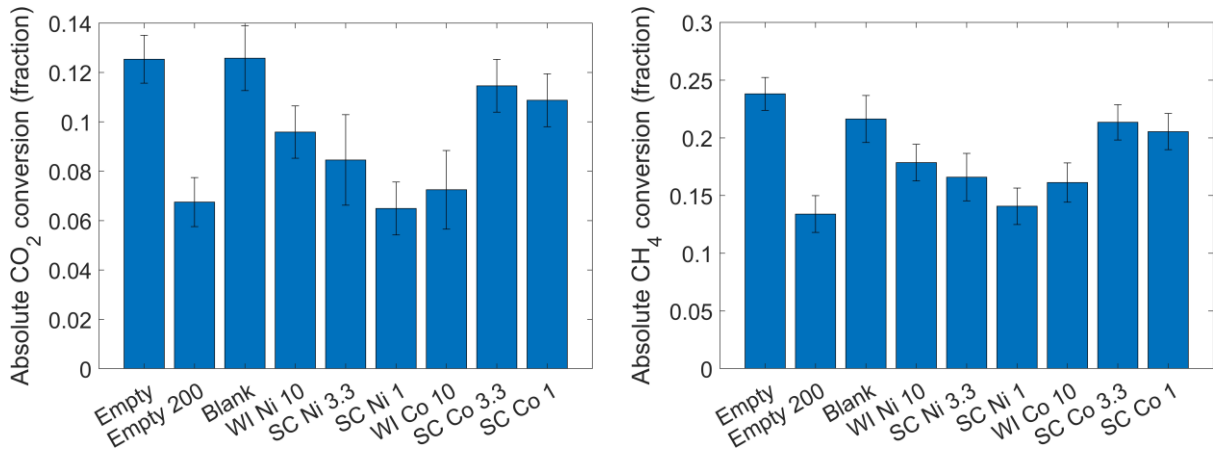
Figure S31: Absolute CO$_2$ conversion (left) and CH$_4$ conversion (right) for DRM with a CO$_2$/CH$_4$ ratio of 1:1
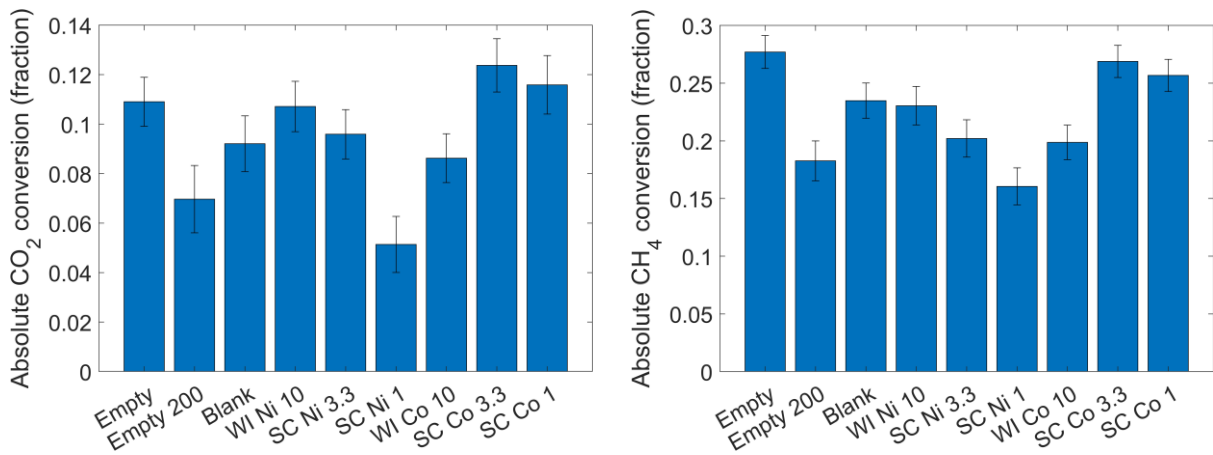

Figure S32: Absolute CO$_2$ conversion (left) and CH$_4$ conversion (right) for DRM with a CO$_2$/CH$_4$ ratio of 2:1
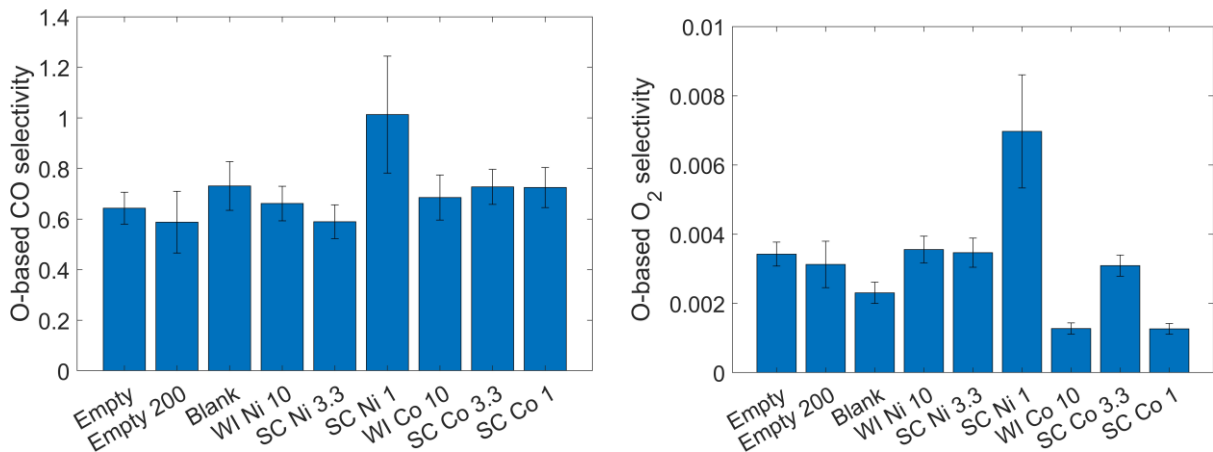

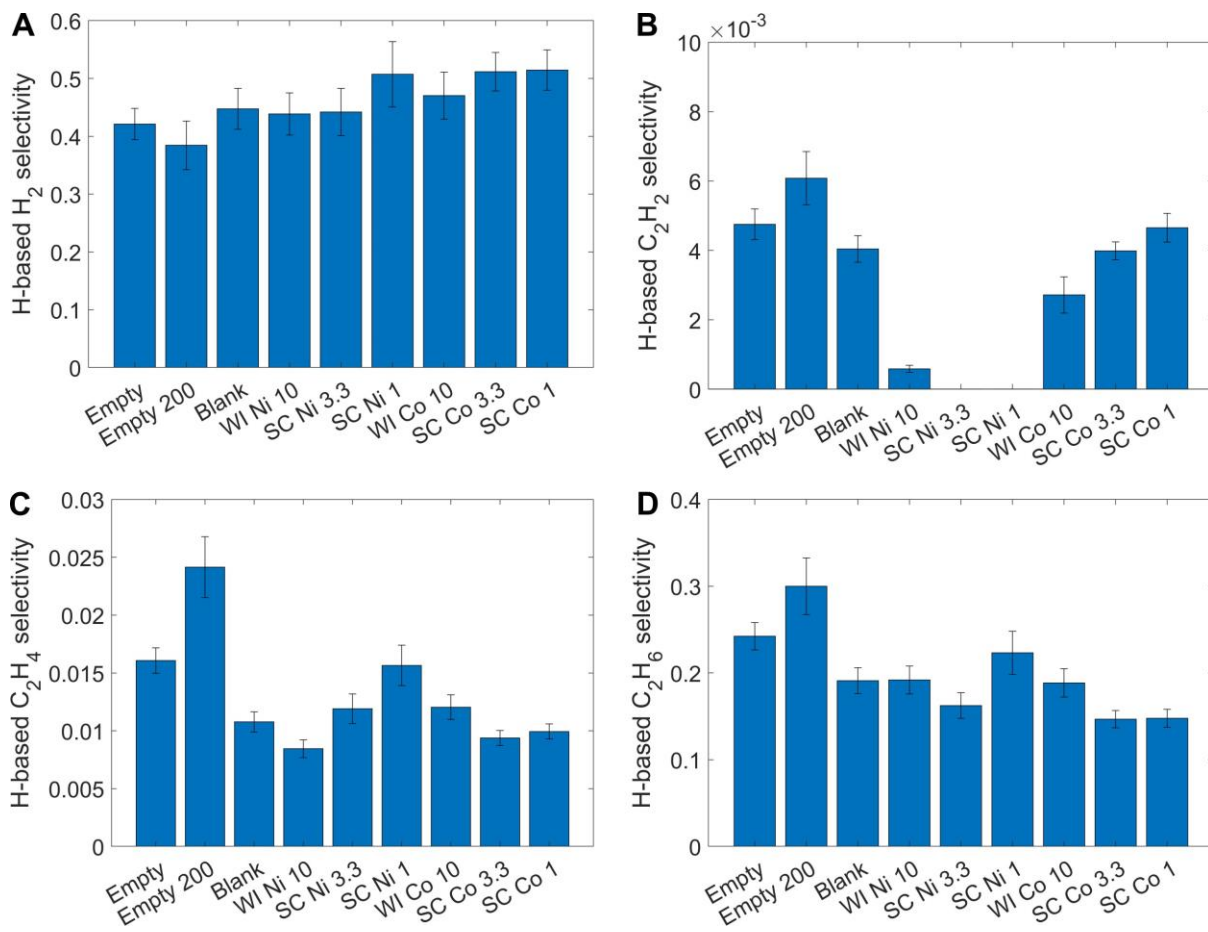*Figure S33: O-based CO (left) and O$_2$ selectivity (right) for DRM with a CO$_2$/CH$_4$ ratio of 2:1*

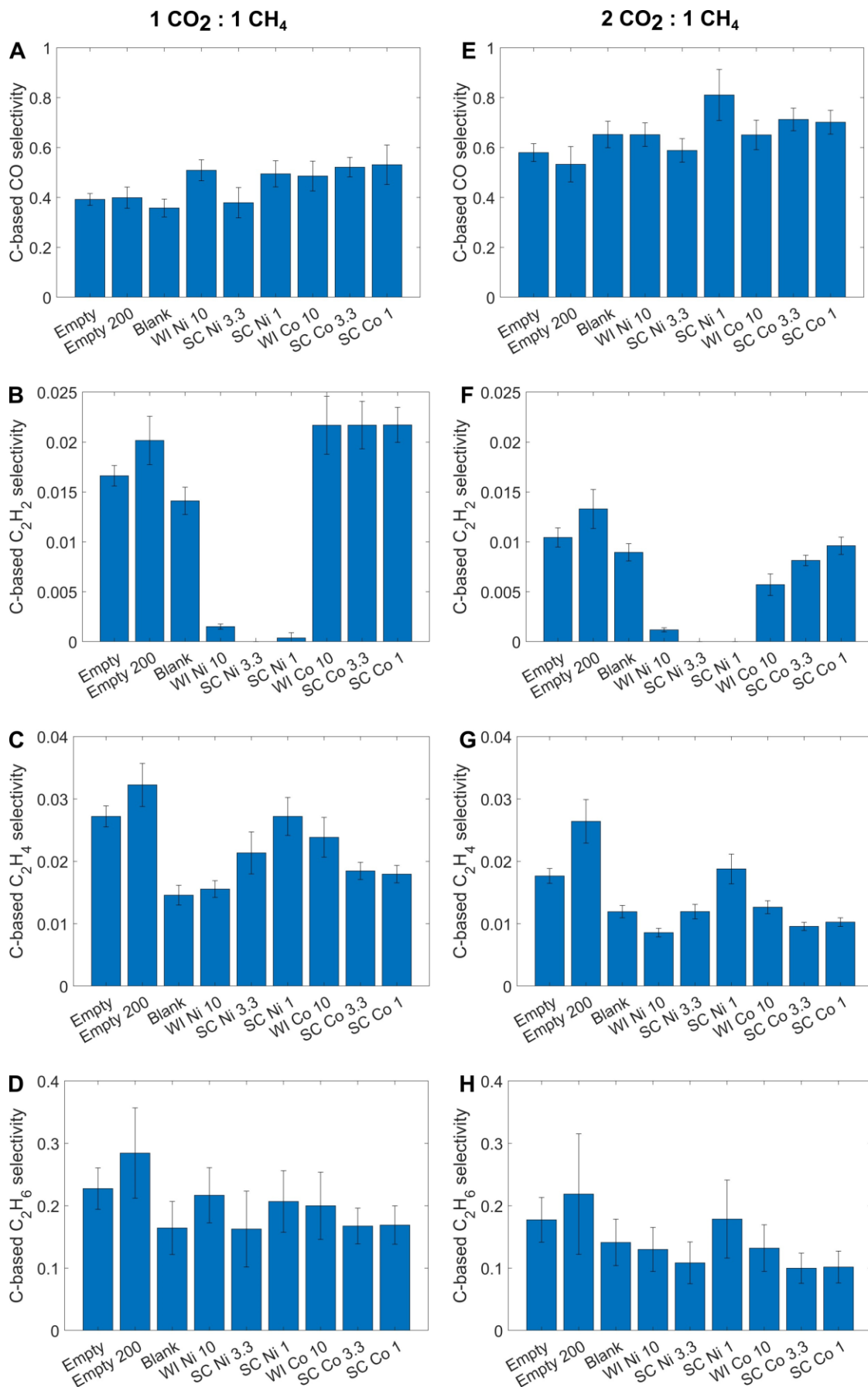*Figure S34: H-based selectivities for DRM with a CO_2/CH_4 ratio of 2:1*

Figure S35: C-based selectivities for DRM with a CO₂/CH₄ ratio of 1:1 (left) and 2:1 (right)
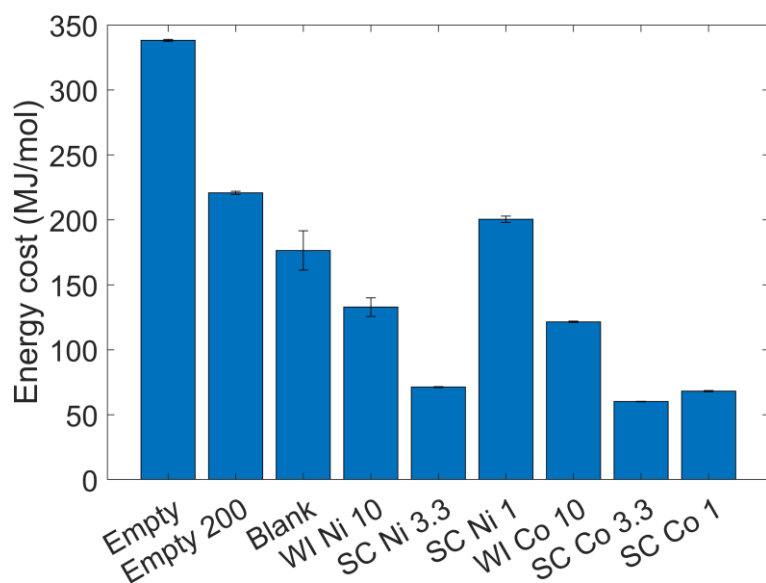
S12.2. NH$_3$ synthesis

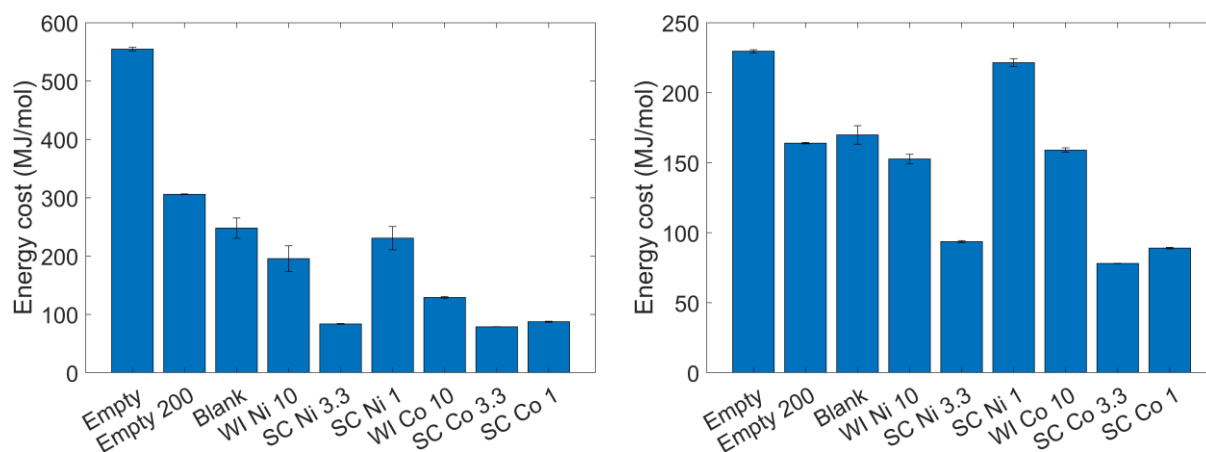*Figure S36:* Energy cost (EC) in MJ/mol NH$_3$ synthesized with a N$_2$/H$_2$ ratio of 1:1

Figure S37: Energy cost (EC) in MJ/mol NH$_3$ synthesized with a N$_2$/H$_2$ ratio of 3:1 (left) and 1:3 (right)